FINAL CONTRACT REPORT

GILES COUNTY, VA PEDESTRIAN BRIDGE COLLAPSE & FAILURE ANALYSIS

Amey Bapat
Graduate Research Engineer

Tommy Cousins
Professor

Ben Dymond
Research Associate

Carin L. Roberts-Wollmann
Associate Professor

Via Department of Civil and Environmental Engineering
Virginia Polytechnic Institute and State University

Project Manager
Jose Gomez, Virginia Transportation Research Council

Virginia Transportation Research Council
(A partnership of the Virginia Department of Transportation
and the University of Virginia since 1948)

Charlottesville, Virginia

June 2009

ABSTRACT

On October 12, 2008, a pedestrian bridge over Walker Creek near Route 749 in Giles County partially collapsed, causing ten people to fall into the creek below. The crossing was a suspension bridge and the collapse occurred when one of the anchor bolts embedded in a concrete dead-man holding a suspension cable fractured. This report presents the investigation of the failure.

The investigation had several components. These components included an analysis of the structure, testing of the remaining section of the broken anchor, testing of the full remaining anchor from the dead-man on the opposite bank of the creek, and calculating the expected strength of the anchor bolt based on tested strength and estimated loading conditions.

The first component was an analysis of the structure to determine the forces that were in the cable and anchor bolt at the time of the collapse. The cable was treated as a simple catenary and the horizontal force in the cable at the tower was calculated. Then, based on measurement of the bridge dimensions, the angles of the back stays could be determined. This angle and the horizontal force were used to arrive at the expected tension force in the cable at the time of failure. The force was calculated to be approximately 6.8 kips considering static loading and 8.6 kips considering dynamic amplification.

The second component was to analyze the bolt to determine the actual properties of the galvanized steel in the bolt. These tests were performed by cutting one tensile coupon and two Charpy test specimens from the retrieved fragment of the broken bolt. In addition, microscopic investigations were undertaken. This analysis was performed by Dr. Bill Wright of the FHWA, and his report is attached as Appendix A. Based on a coupon cut from the center of the bolt, it was determined that the specimen has a yield strength of 55 ksi and an ultimate strength of 88 ksi. However, based on Vickers hardness tests, it was shown that the strength of the material near the surface was significantly higher due to strain aging associated with the hook bend. The other important finding was that a small flaw existed at the inside bend of the hook, and it is very likely that this flaw resulted in the hook experiencing a brittle failure after the onset of ductile yielding.

The next component was to test the hook that was anchoring the same cable as the ruptured anchor bolt, but was located on the opposite bank of the creek. This hook was taken to the laboratory and tested in such a manner as to load the hook with the same eccentricity that was observed in the field, 1 ½ in. The results of this test indicated that non-linear behavior initiated at a load of 7 kips, and the cross-section was fully yielded at load of 11.9 kips.

The final component was to evaluate the strength of the bar under combined axial force and moment and compare the calculated strength to the calculated force in the hook at the time of rupture. This analysis confirmed the conclusions of Dr. Wright. The hook was expected to have experienced some yielding, but had not experienced the full load calculated to cause rupture. Therefore, the flaw must have triggered a premature failure. It was also interesting to observe that the single cable remaining, carrying the full dead load of the bridge, is carrying a larger load than each cable carried when they were working together to carry dead load plus live

load. The two hooks anchoring the remaining cable are still intact, although they exhibit evidence of inelastic behavior.

In conclusion, the anchor rod would have had more than adequate capacity to carry the loads on the bridge on the day of failure, even considering dynamic load amplification caused by swinging or shaking the bridge, if there had been no eccentricity of load on the hook. With the hook eccentricity, the anchor still was adequate if there had been no flaws in the material. The presence of the flaw, the eccentricity of the load, and the higher than typical pedestrian loads, with dynamic amplification, all contributed to the failure of the anchor rod and the partial collapse of the bridge.

FINAL CONTRACT REPORT

GILES COUNTY, VA PEDESTRIAN BRIDGE COLLAPSE & FAILURE ANALYSIS

Amey Bapat
Graduate Research Engineer

Tommy Cousins
Professor

Ben Dymond
Research Associate

Carin L. Roberts-Wollmann
Associate Professor

Via Department of Civil and Environmental Engineering
Virginia Polytechnic Institute and State University

INTRODUCTION

On October 12, 2008, a pedestrian bridge over Walker Creek near Route 749 in Giles County partially collapsed, causing ten people to fall into the creek below. The crossing was a suspension bridge and the collapse occurred when one of the anchor bolts embedded in a concrete dead-man holding a suspension cable fractured. This report presents the investigation of the failure.

Description of Bridge

The pedestrian bridge over Walker Creek is a suspension bridge with a 160 ft main span. Figure 1 shows the bridge after failure. The suspension cables are 1 in. in diameter. At each end of each cable, the cable is attached to a 1 in. diameter galvanized steel bar, bent into a closed hook and embedded in a large concrete dead-man. The floor beams are spaced every 5 ft, and are rough cut 4 x 4s. It is believed that all timber components of the bridge are treated pine. Two stringers are supported by the floor beams. The stringers are rough cut 2 x 4s, and they appear to be 12 ft long, lapped at every other floor beam (see Figure 2). The decking is rough cut 1 x 6s approximately 36 in. long, spanning across the stringers. The suspender cables are 3/8 in. diameter cables, and the bridge has a wire mesh guard fence on each side.

Figure 1. Giles County Pedestrian Bridge.

Figure 2. Detail of Flooring System.

The bridge is inspected every two years by a bridge inspection crew from the Salem District of the Virginia Department of Transportation (VDOT). The most recent inspection was conducted in May 2007 (VDOT 2007) and it was reported that each of the condition ratings were good for the 3 specific items, i.e. the foot bridge anchorage, the deck, and the superstructure.

Anchor rods were viewed and verified as good. The signage was verified as in place. The sign is shown in Figure 3.

Figure 3. Intact sign located at each end of bridge.

The bridge inspection crew from the Salem District provided measurements of the existing bridge. The investigators were also provided with the general plan sheets that were likely used for the construction of this bridge. With this information, an as-built drawing of the bridge was constructed. It is presented in Figure 4.

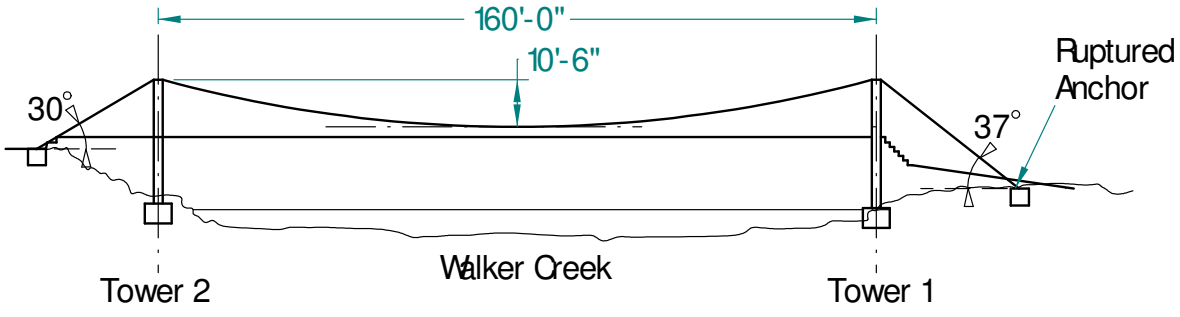

Figure 4. Dimensions Used for Analysis of Suspension Bridge.

Scope

The investigation had several components, namely:

- An analysis of the structure to determine expected forces in the anchor rods at the time of collapse
- Testing of the remaining section of the broken anchor to determine the actual properties of the galvanized steel in the rod
- Testing of the full remaining anchor from the dead-man on the opposite bank of the creek
- Calculation of the expected strength of the anchor bolt based on tested strength and estimated loading conditions

The first component was an analysis of the structure to determine the forces that were in the cable and anchor bolt at the time of the collapse. The cable was treated as a simple catenary and the horizontal force in the cable at the tower was calculated. Then, based on measurement of the bridge dimensions, the angles of the back stays could be determined. This angle and the horizontal force were used to arrive at the expected tension force in the cable at the time of failure.

The second component of the investigation was to analyze the bolt to determine the actual properties of the galvanized steel in the bolt. These tests were performed by cutting one tensile coupon and two Charpy test specimens from the retrieved fragment of the broken bolt. In addition, microscopic investigations were undertaken. These investigations included optical examination with a digital microscope and more detailed examination with a scanning electron microscope. This analysis was performed by Dr. Bill Wright of the FHWA, and his report is attached as Appendix A. He also investigated the Vickers hardness of the material across the cross-section of the bar.

The next component of the investigation was to test the hook that was anchoring the same cable as the ruptured anchor bolt, but was located on the opposite bank of the creek. Before the anchor bolt was cut, at the point where it exited the dead-man, it was noted that the originally closed hook had opened; furthermore, one of the hooks anchoring the remaining cable had also opened. There was an observable eccentricity of the cable load relative to the center line of the hook, as shown in Figure 5. The retrieved hook was taken to the laboratory and tested in such a manner as to load the hook with the same eccentricity that was observed in the field, 1 ½ in.

The final component was to evaluate the strength of the bar under combined axial force and moment and compare the calculated strength to the calculated force in the hook at the time of rupture. These calculations were performed based on the material strengths provided by Dr. Wright.

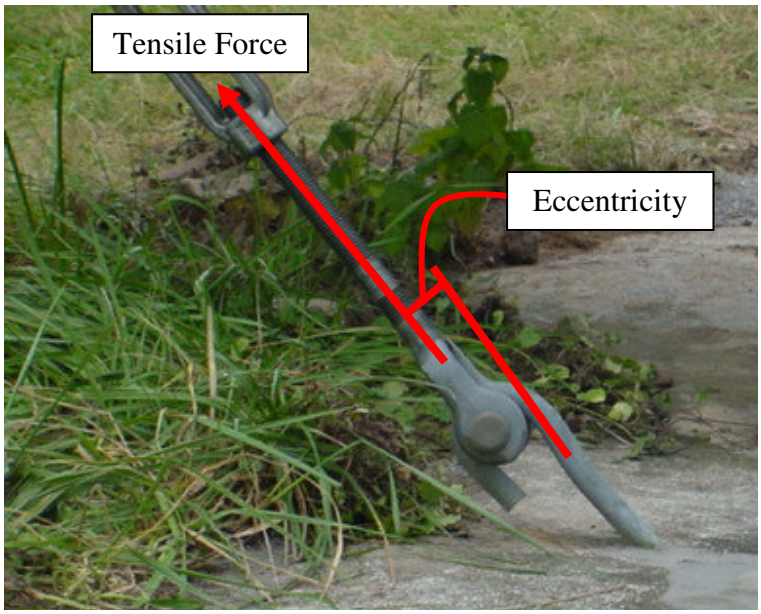

Figure 5. Anchor Geometry and Eccentricity

METHODS

Suspension Bridge Analysis

Cable Force Calculation

Maximum tension in a cable subjected to uniformly distributed load can be determined using Equation 1. (Hibbeler 2004).

$$T_{max} = w_o \times L \times \sqrt{1 + \left(\frac{L}{2f}\right)^2} \qquad \text{Equation 1}$$

where:

T_{max} = maximum tension in the cable, at the tower
w_o = uniformly distributed load
L = one half the projected length of the cable on the x-axis
f = maximum cable sag

For the Giles County Bridge, the total span length was 160 ft, so L = 80 ft, and the sag, as determined by the surveyors, was 10.5 ft.

The tension in the suspension cable after it passes over the tower can be calculated by two different methods:

1. Tension in the cable over the saddle remains constant assuming that there is no loss due to friction as it passes over saddle.

2. Horizontal force in the cable remains constant assuming that there is no loss due to friction and the horizontal stiffness of the tower is very small as compared to the stiffness of the suspension cable.

The second method was used in the calculation of the force in the cable as it will result in higher tensile force on the back stay side of the tower for this suspension bridge.

The horizontal force at any point on a cable subjected to a uniform load can be calculated as follows:

$$F_H = \frac{w_o x^2}{y} \qquad \text{Equation 2}$$

where:

F_H = horizontal force in cable
x = distance along cable, measured from center of span
y = height of cable above low point at center of span

At the tower, x = 80 ft, and y = 10.5 ft.

Once the horizontal force at the tower is known, the tension in the back stay is calculated as:

$$T = \frac{F_H}{\cos\theta} \qquad \text{Equation 3}$$

where:

θ = angle of backstay, relative to horizontal

For the Giles County Bridge, the angle of the backstay at the fractured anchor was approximately 37 degrees, which is the more critical case in terms of maximum tension force. At the opposite dead-man, the angle was approximately 30 degrees.

Dead Load Calculation

To determine the tension force, it was first necessary to estimate the dead load on the bridge. The dead load was the sum of the weights of the cable, hangers, floor beams, stringers, decking and fencing. This section presents the assumptions made and the resulting dead load calculations.

The cable was 1 in. diameter steel, so a conservative estimate of self weight is 2.67 lb/ft. Since there were two cables, the total load was 5.34 lb/ft.

The suspenders were 3/8 in. diameter wire rope. Based on field measurements, the average suspender length was 86 in., and the suspenders were spaced every 5 ft along the span. The average weight of one suspender was 2.68 lb, so the distributed load, for hangers on both sides of the bridge, was 1.1 lb/ft.

The floor beams were rough cut 4 x 4's, 48 in. long, spaced at 5 ft c-c. It is not known what type of wood the floor beams were, but it is assumed to be a treated pine. For calculations,

the wood was assumed to have a unit weight of 40 lb/ft^3. The floor beams weighed about 18 lb each, so the distributed load from the floor beams was 3.6 lb/ft.

The stringers were rough cut 2 x 4's, 12 ft long, lapped approximately every 10 ft. The lap splicing of the stringers can be seen in Figure 3. It was also assumed that a treated pine was used for the stringers. As for the floor beams, the unit weight was assumed to be approximately 40 lb/ft^3. Therefore, the distributed load of two 2 x 4 stringers was 4.44 lb/ft. This was increased by 10 percent to 4.9 lb/ft to account for the splicing.

The decking was rough cut 1 x 6 planks, 36 in. long. It was also assumed that the wood was treated pine, with a unit weight of 40 lb/ft^3. The decking resulted in 10 lb/ft of dead load.

The guard fence was 36 in. high and appeared to be No. 9 Ga. woven wire. Based on information from the Direct Metals website (www.directmetals.com), a unit weight of 2.9 lb/ft was estimated.

Based on the above described assumptions, the total distributed dead load on the bridge was 27.8 lb/ft.

Live Load

Two different live loads are used in the calculations of cable forces. The first is the estimated live load on the bridge at the time of the collapse. The eye witness reports indicate that there were 10 people on the bridge prior to failure. It is unknown what the weight of each individual was, but the assumption was made that the average weight was 170 lb/person. For 10 people on the 160 ft span, the resulting live load is 10.63 lb/ft.

The second live load that was used for comparison purposes is the design live load as listed on the bridge drawings. The notes on the drawing stipulate a 16 lb/ft distributed live load.

The drawings also indicate that an impact factor of 100 percent should be assumed. This is a reasonable factor to be used in analysis, and it accounts for the dynamic amplification of the forces caused by swinging or shaking the bridge.

Testing the Fractured Anchor Rod

Figure 6 shows the fractured anchor rod shortly after the bridge collapse. Figure 7 shows a close-up view of the fractured surface of the anchor rod. The rod appears to have fractured at the widest point of the hook. VDOT crews searched for the missing portion of the hook, but it could not be located. The rod was saw cut as close to the concrete dead-man as possible so the specimen could be analyzed. The bar was sent to Dr. Bill Wright of the FHWA.

Figure 6. Fractured Anchor Rod

Figure 7. Cross section view of fractured anchor rod

Dr. Wright's report is presented as Appendix A, so the details of the testing are not presented herein. The important results from his tests include the stress-strain behavior of the steel, the hardness testing, and the microscopic investigation.

Anchor Rod Laboratory Testing

The goal of the laboratory test setup was to reproduce the loading conditions experienced by a typical cable anchor rod at the Giles County footbridge. This involved pulling the anchor in tension while inducing a moment in the specimen due to the geometry of the anchor as shown in Figure 5. The eccentricity from the line of action of the tensile force to the centerline of the anchor body was measured to be approximately 1 ½ in.

It was deemed more practical to setup the laboratory test in a horizontal plane rather than try to exactly match the angled cable and bridge geometry. Figure 8 and Figure 9 show the laboratory test setup in elevation and plan view, respectively. A threaded rod load cell was used to measure the applied tensile load during testing of the anchor rod. The threaded rod was connected to an end of the Giles County footbridge turnbuckle using a coupling nut. This line of action, including the threaded rod and turnbuckle, was offset from the centerline of the anchor rod shaft to maintain the 1 ½ in. of eccentricity that was present in the field. The turnbuckle was then connected to the anchor rod using the pin from the Giles County Bridge. To ensure that the anchor maintained 1 ½ in. of eccentricity, the anchor rod shaft was welded to an inverted steel T-shape, shown in Figure 10, which was then bolted and centered on the strong floor in the laboratory.

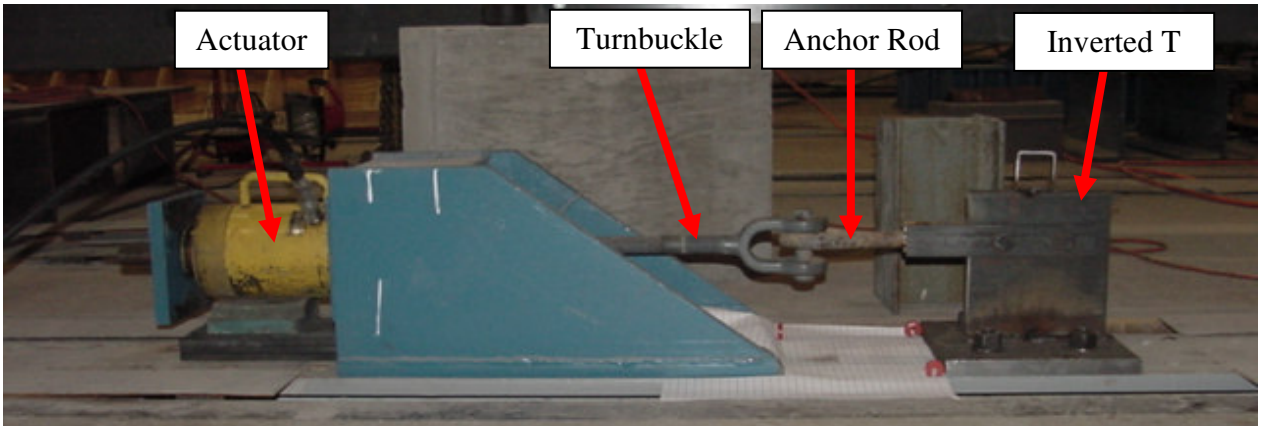

Figure 8. Section View of Laboratory Test Setup

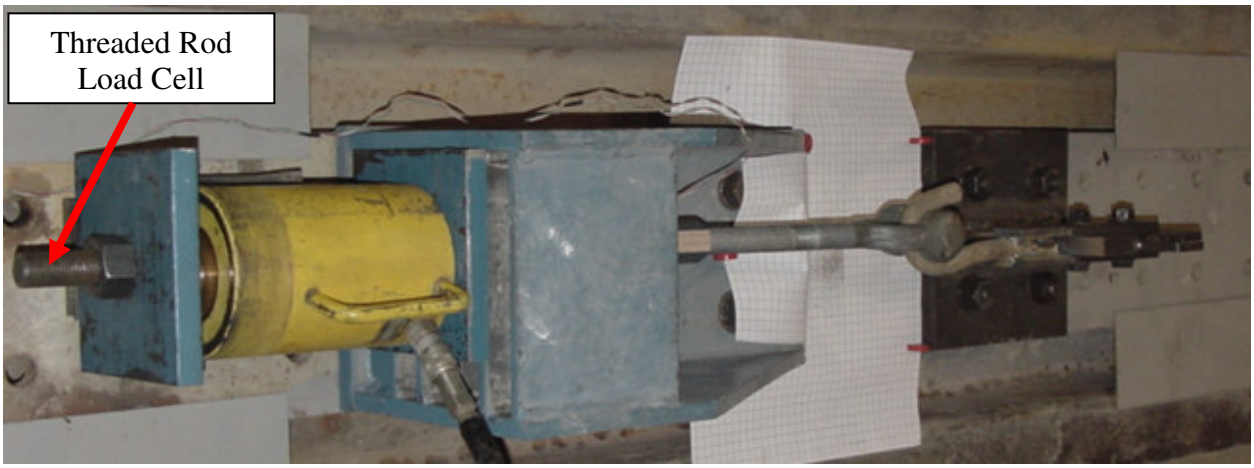

Figure 9. Plan View of Laboratory Test Setup

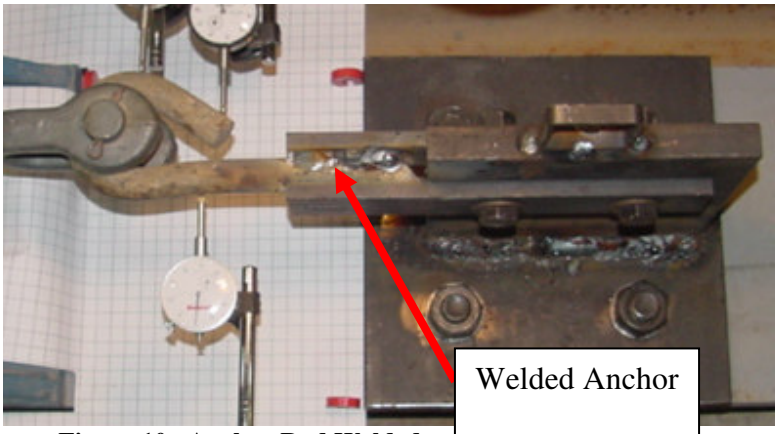

Figure 10. Anchor Rod Welded to Inverted Steel T-Shape

Instrumentation, shown in Figure 11, was used in the test setup to measure tensile force, displacement, and deformation. A threaded rod load cell measured the in-line tensile force in pounds, and the linear displacement of the threaded rod was measured in inches using a dial gage. Three additional dial gages were used to measure the displacement and deformation of the anchor rod hook.

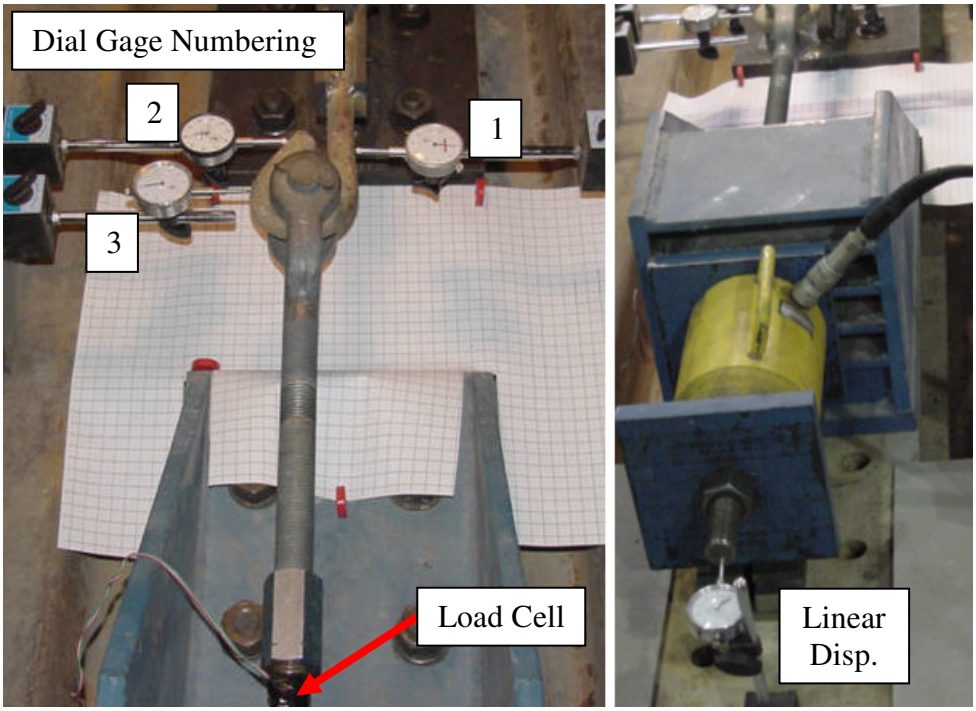

Figure 11. Dial Gage Instrumentation

Finally, the anchor rod deformation and change in geometry over time was monitored using a sheet of graph paper with a ½ in. grid, shown in Figure 11, and a video camera focused on the hook. The graph paper was centered under the hook and the camera was setup on a tripod looking directly down on the hook to monitor the change in geometry over time. The three dial gages, graph paper, and video camera allowed close monitoring of how the hook opened over time as tensile force was applied and moment was induced in the anchor rod.

Strength of Rod under Combined Axial Force and Moment

Based on field observations, because the anchor hook was not closed and welded, the most critical location on the hook is at the widest point. At this location, the rod is subjected to both a high axial force and a significant moment. To determine if the loads on the bridge would be expected to result in failure of the rod, it was necessary to construct a moment-axial force interaction diagram for the rod. This analysis was performed to assess several possible stress levels in the rod. The four analyses performed included:

- Moment and axial force combinations to result in first yield, based on 55 ksi yield,
- Moment and axial force combinations to result in yielding of the full cross-section, based on 55 ksi yield,
- Moment and axial force to result in yielding of the full cross-section considering increased yield strength as determined by Wright,
- Moment and axial force to result in near ultimate strength across the section with strengths as determined by Wright.

Elastic Method

The first analysis of the anchor rod is carried out using the elastic method and AISC LRFD design provisions for members subjected to combined bending and tension. This method is valid only for the elastic portion of the stress strain curve and it can predict the first yield at the extreme outer fiber of the cross section. Combinations of axial force and moment that are at or below first yield satisfy Equation 4

$$\frac{P_r}{P_c}+\left(\frac{M_{rx}}{M_{cx}}+\frac{M_{ry}}{M_{cy}}\right)\le 1.0 \qquad \textbf{Equation 4}$$

where:

P_r = required tensile strength
P_c = F_yA_g =design tensile strength
A_g = gross cross-sectional area
M_r = required flexure strength
M_c = f_yS = moment at first yield
S = elastic section modulus
F_y = yield stress

AISC LRFD Design Method

The second method of analysis uses perfect elastic-plastic stress strain relationship for steel. More refined analysis can be carried out using the actual stress strain curve obtained from test results. Currently, the AISC 13th edition calculates the capacity of a doubly symmetric member in flexure and torsion using Equation 5 and Equation 6, as follows:

For $P_r / P_c \ge 0.2$

$$\frac{P_r}{P_c}+\frac{8}{9}\times\left(\frac{M_{rx}}{M_{cx}}+\frac{M_{ry}}{M_{cy}}\right)\le 1.0 \qquad \textbf{Equation 5}$$

For $P_r / P_c < 0.2$

$$\frac{P_r}{2P_c}+\left(\frac{M_{rx}}{M_{rc}}+\frac{M_{ry}}{M_{cy}}\right)\le 1.0 \qquad \textbf{Equation 6}$$

where:

P_r = required tensile strength using LRFD load combination, kips
P_c = $\phi_t P_n$ =design tensile strength, kips
P_n = minimum of F_yA_g and F_uA_e
A_g = gross cross-sectional area
A_e = effective net area

M_r = required flexure strength using LRFD load combination, kips
M_c = $\phi_b M_n$ = design flexural strength
M_n = $F_y Z \leq 1.6 M_y$ i.e $1.6 F_y S$
Z = plastic section modulus
S = elastic section modulus
F_y = yield stress
F_u = ultimate stress
ϕ_t = resistance factor for tension
ϕ_b = resistance factor for bending

Since this was an analysis problem, and not a design problem, the strength reduction factors were considered to be 1.0.

Analysis Considering Increased Yield Strength

The material testing performed by Wright included tension testing of a reduced size coupon taken from the center of the rod. This testing indicated that the yield strength was 55 ksi and the ultimate strength was 88 ksi. These values were used in the first two analysis methods. However, Wright also performed Vickers hardness testing across the cross-section. This testing revealed that the material had considerably higher strength near the surface than at the center of the bar. The tests indicated that the yield strength at the surface was close to 79 ksi and the ultimate tensile strength near the surface was 128 ksi.

A simplified analysis was performed to determine how much additional strength might be realized in the rod due to the higher strengths at the exterior of the section. Figure 12 shows how the cross-section was divided into five individual sections. Each section was assigned a yield strength according to the hardness profile in Wright's report. The axial strength, if all sections have reached yield, is simply the sum of the areas of the sections times its yield stress. The flexural strength is the sum of the plastic section modulus of each section times its yield strength. The assumption of a fully plasticized cross-section is reasonable based on the stress-strain diagram produced by Wright, based on his tensile coupon test. The yield plateau for the material extended to a strain of 0.012 before the onset of strain hardening. For this analysis, the interaction diagram was assumed to be a straight line between the point of pure axial force and the point of pure moment.

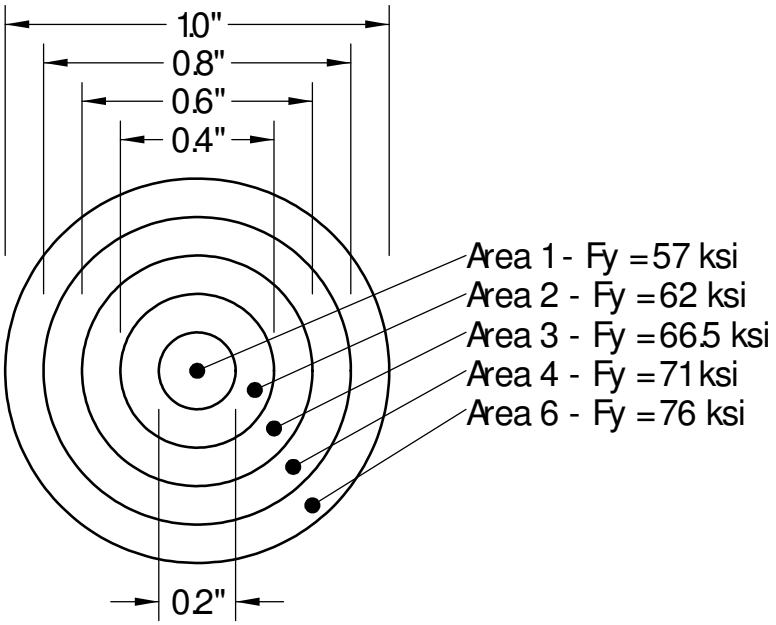

Figure 12. Divided Cross-section for Analysis Considering Increased Yield Strength

Analysis Considering Increased Ultimate Strength

An analysis similar to that described in the previous section was undertaken, except the ultimate strengths were used rather than the yield strengths. The stress-strain diagram presented by Wright indicated that there was a section of the plot within the strain-hardening portion of the curve, where a constant stress, approximately equal to the ultimate strength, was maintained through a large strain increase. This plateau region was between approximately 75000 με and 175000 με. Based on this observation, it could be assumed that a large portion of the cross-section could be on this plateau at a given load. The ultimate strengths assigned to the areas are presented in Table 1.

Table 1. Ultimate Strengths Assigned to Areas in Figure 10.

Area Designation	Ultimate Strength, ksi
1	88
2	100
3	108
4	116
5	124

RESULTS

Suspension Bridge Analysis

Using the methods described previously, Table 2 presents the calculated tension in the cable based on a variety of loading conditions.

Table 2. Calculated Cable Tensions

Load Combination	Dead Load per Cable, lb/ft	Live Load per Cable, lb/ft	Total Load per Cable, lb/ft	Horizontal Force, kips	Force in 37° Back Stay, kips	Force in 30° Back Stay, kips
DL + Design LL (static)	13.9	8	21.9	6.67	8.35	7.70
DL + Design (LL + I)	13.9	16	29.9	9.11	11.41	10.52
DL + Estimated LL (static)	13.9	5.3	19.2	5.85	7.33	6.76
DL + Estimated (LL + I)	13.9	10.6	24.5	7.47	9.35	8.63
DL on one cable	27.7	0	27.7	8.44	10.57	9.75

It is interesting to note that the one cable that remains, carrying the full dead load of the bridge, has a calculated force in the back stay larger than the value calculated based on the assumed live load plus impact on the bridge at the time of collapse. Observations at the bridge site indicate that other components, such as the 3/8 in. diameter cable at the top of the safety fencing, and the continuous stringers, may be carrying part of the dead load with catenary action. This would reduce the force in the remaining cable.

Testing the Fractured Anchor Rod

Appendix A presents the report prepared by Dr. Bill Wright on the material properties of the fractured anchor rod. He reported that the material appeared to be an ASTM F 1554 Grade 55 anchor bolt steel, galvanized. The tested yield strength was 54.2 ksi and the ultimate tensile strength was 88 ksi. As noted previously, Vickers hardness testing indicated that the rod had a higher tensile and yield strength closer to the surface.

The other important conclusion came from microscopic investigations. There was a small defect at the fractured surface (Figure 7 shows this defect located at the surface of the lower edge of the rod). This flaw is likely to have triggered the brittle failure of the rod. However, fracture appears to have been preceded by yielding at the inside of the hook.

Anchor Rod Laboratory Testing

The goal of the laboratory test setup was to reproduce the loading conditions experienced by a typical cable anchor rod at the Giles County footbridge. This was achieved in the test setup previously described; testing of the sample anchor rod took place on November 17, 2008 and lasted for approximately one hour.

During the test, the load was increased in 1,000 lb increments, proceeding until 5,000 lb of tension were applied to the anchor rod. After this point, the load was increased in 500 pound increments from 5,000 lb to 10,000 lb of tension. Finally, the load was increased in 250 pound increments from 10,000 lb until the final load of 11,900 lb of tension was reached. At each load increment, measurements of linear displacement of the threaded rod load cell were recorded. A plot of approximate load vs. deflection can be seen in Figure 13. Additionally, Figure 13 highlights certain loads that correspond with a frame from the video taken during testing. All of the video frames are shown Figure 14(a) through Figure 14(i). The load is taken as approximate due to loss of hydraulic pressure and slight decreases in load as dial gage measurements were taken.

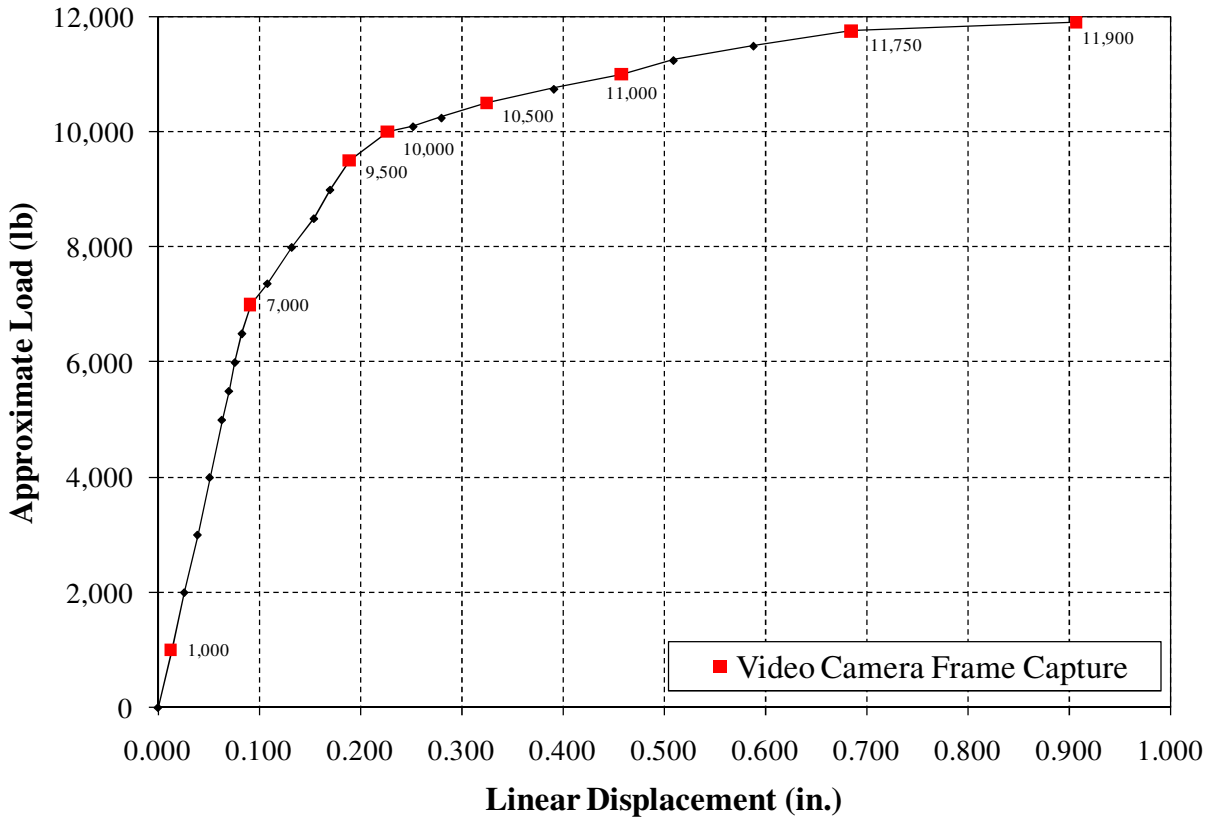

Figure 13. Load vs. Linear Displacement

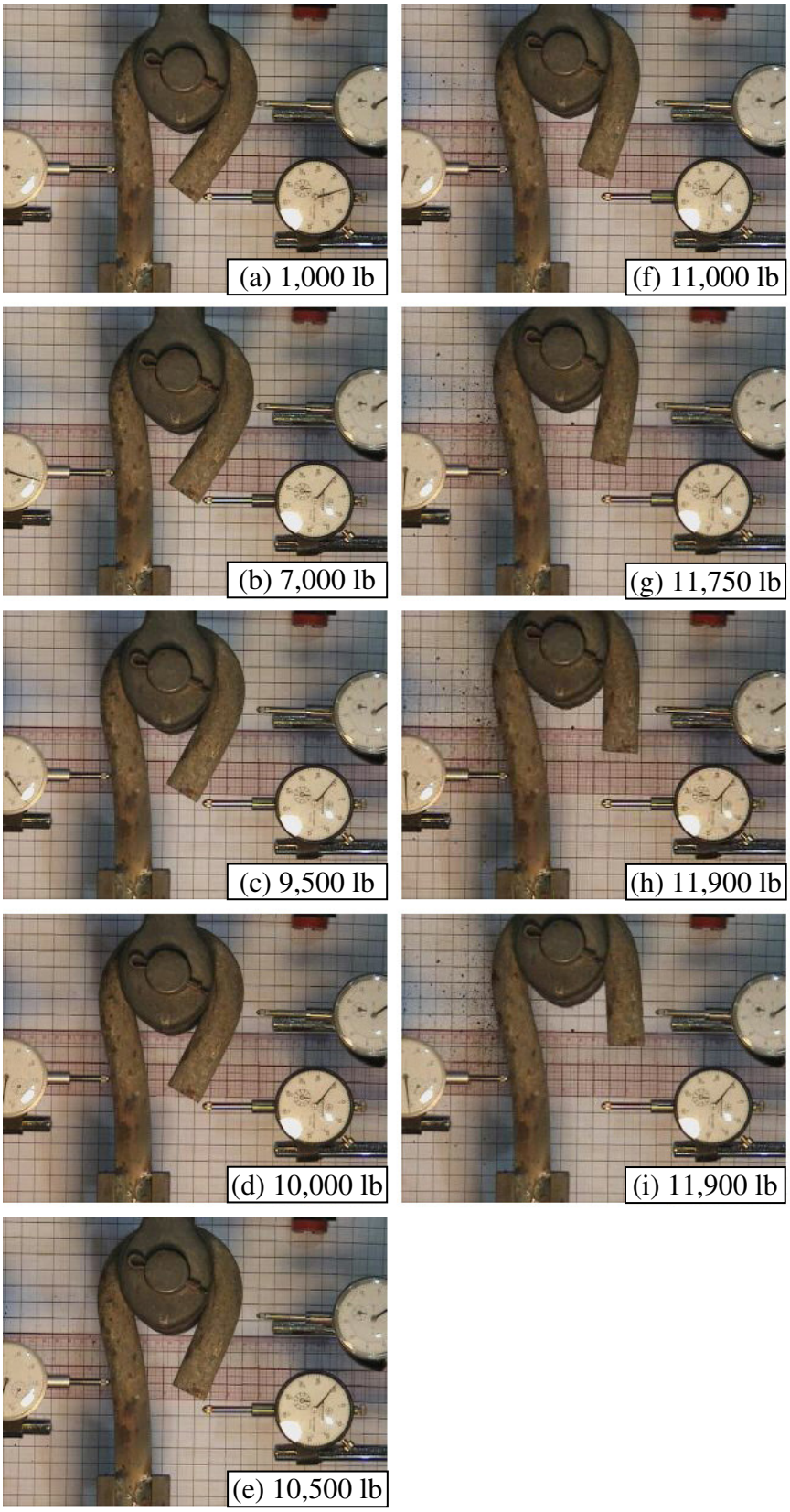

Figure 14. Frames from Testing Video and Corresponding Load

Figure 14 displays how the anchor rod hook deformed as the load was increased with frames from the video corresponding to selected loads. The frame pictures highlight the overall behavior of the hook as tension and the corresponding induced moment are applied to the specimen. Figure 14 (a) is a frame from the beginning of the test with all of the dial gage instrumentation recording deformation values. A close look at the graph paper in Figure 14 (a) shows the gap at the end of the hook is approximately ½ in. Figure 14 (b) shows dial gage 3 is no longer touching the anchor rod; this is due to the fact that the anchor rod is straightening and starting to un-hook. This effect is evident both in Figure 14 (c) and in Figure 15. In Figure 14 (c) dial gage 2 is no longer touching the hook, and in Figure 15 the displacement measured by both dial gage 2 and dial gage 3 are vertical lines indicating they are no longer in contact with the anchor rod hook. Also evident in Figure 15 is that the dial gages stopped measuring displacement prior to a load of 7,000 lb as is indicated in Figure 14. The plotted values of dial gage displacement show dial gage 2 stopped measuring displacement at approximately 4,000 lb and dial gage 3 stopped measuring displacement at approximately 1,000 lb.

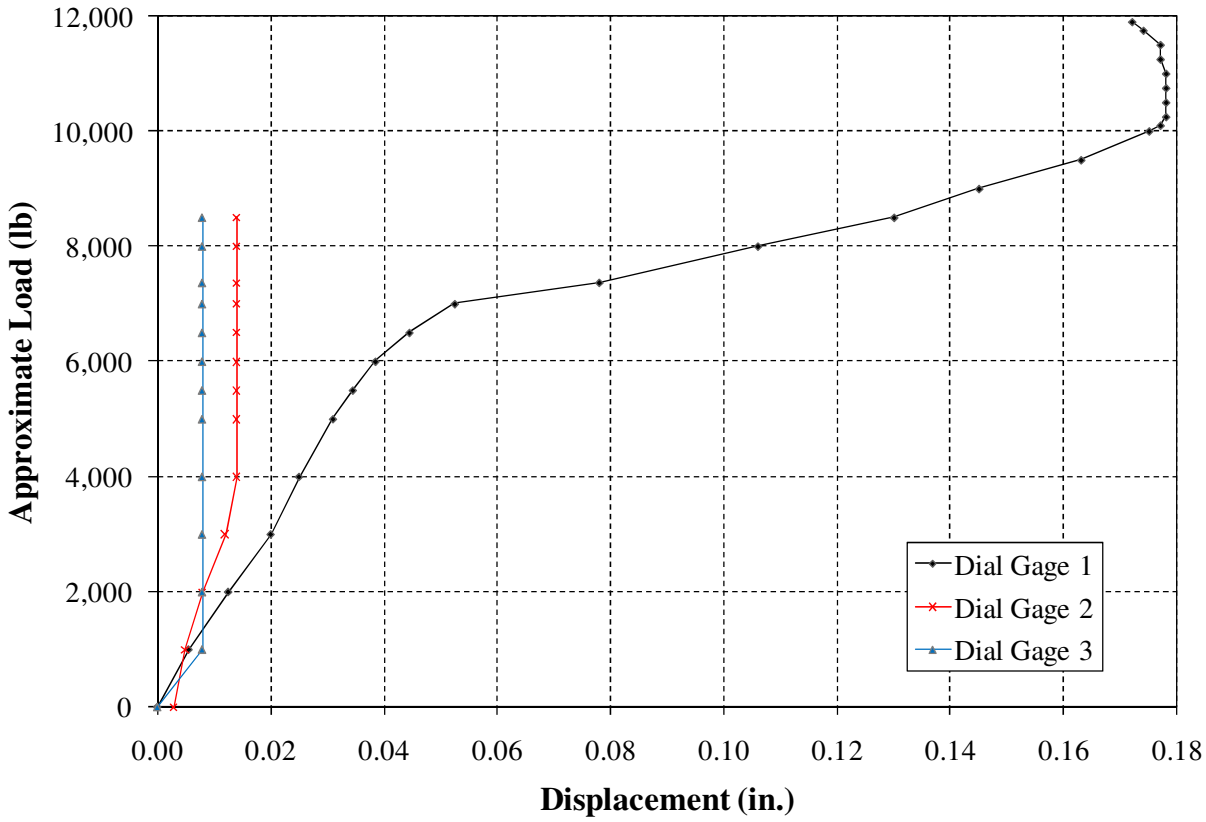

Figure 15. Load vs. dial Gage Displacement

Figure 14 and Figure 15 also display how the anchor hook opened with increasing load. Figure 15 exhibits this trend as dial gage 1 indicates large increases in displacement from 1,000 lb to 10,000 lb. Through this time period, the shaft of the anchor rod is straightening while the hook of the anchor maintains relatively the same shape (as shown in Figure 14 (a) through (c)). Finally, the anchor achieved some equilibrium at approximately 10,000 lb as dial gage 1 exhibits more of a straight vertical line.

From Figure 14 (d) through (i), 10,000 lb through the final load of 11,900 lb, it is evident that the hook of the anchor rod is opening and attempting to straighten. Figure 14 (h) and (i) are both video camera frames at a load of approximately 11,900 lb. During the time period between these two frames, the hydraulic ram was still pulling the anchor rod in tension and opening the specimen's hook, but the load was no longer increasing beyond the maximum load shown in Figure 13. The investigators believe that this is the ultimate behavior of the anchor rod and hook over time. Any attempt to add additional load would lead to more deformation in the anchor rod hook (a straightening or opening behavior). Figure 14 (i) and Figure 16 show that the final gap between the shaft of the anchor rod and the hook, measured with the graph paper, is approximately 2 in. Additionally, Figure 17 shows the typical behavior of the anchor rod as it is attempting to straighten. The final eccentricity of the line of action from the turnbuckle to the anchor rod shaft was measured to be approximately ¾ in. as compared to the original eccentricity of approximately 1 ½ in. shown in Figure 14 (a). However, the maximum eccentricity is still 1 ½ in., measured from the centerline of the turnbuckle pin to the center of the bar at the widest point of the hook.

Figure 16. Final Anchor Rod Hook Geometry

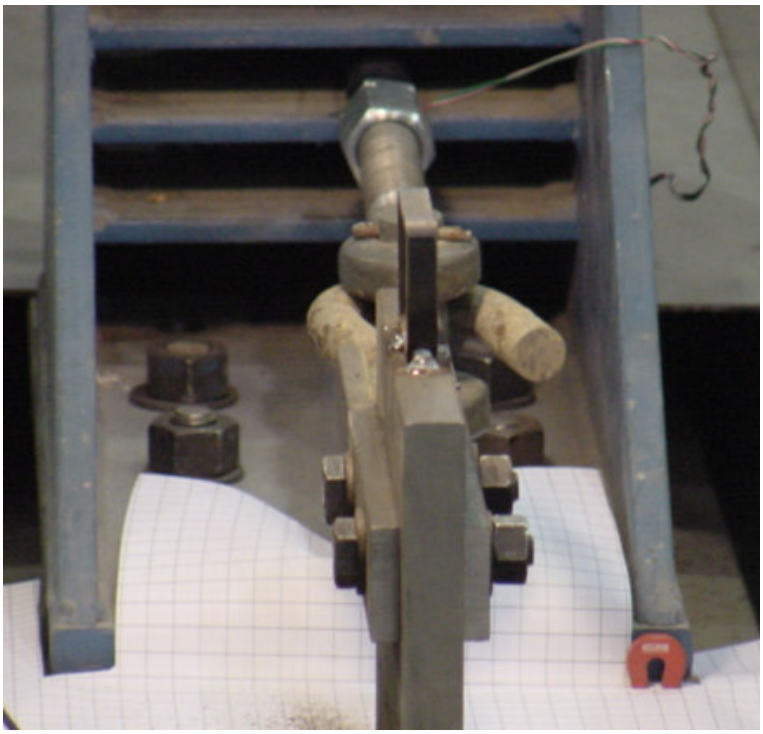

Figure 17. Anchor Rod at End of Testing

Strength of Rod under Combined Axial Force and Moment

Based on the processes described in the Methods section, four moment-axial force interaction diagrams were constructed. They are presented in Figure 18. Also shown on the plot are several points indicating force and moment combinations on the anchor rod at the bridge site and during laboratory testing.

Note that the first point from the testing program was at a load of 7 kips and a moment, assuming a 1 ½ in. moment arm, of 10.5 in-kips. This falls very close to the interaction line calculated based on full yielding of the cross-section considering increased yield strengths as determined by Wright. During testing, at 7 kips the specimen started to show non-linear behavior, based on the deformation in the direction of the applied load (see Figure 13) and based on deformation perpendicular to the applied load (see Figure 15, dial gage 1). The observation that inelastic behavior was not apparent at lower loads, closer to the first yield line in Figure 18, supports Dr. Wright's conclusion that the rod had higher yield strength at the surface than at the center of the rod.

Also note that the second point from the testing program was at a load of 11.9 kips and a moment, also assuming a moment arm of 1 ½ in., of 17.9 in-kips. This point falls outside the interaction line. The test was halted because it was believed that the rod was very close to rupture, and this is confirmed by its proximity to the failure interaction line.

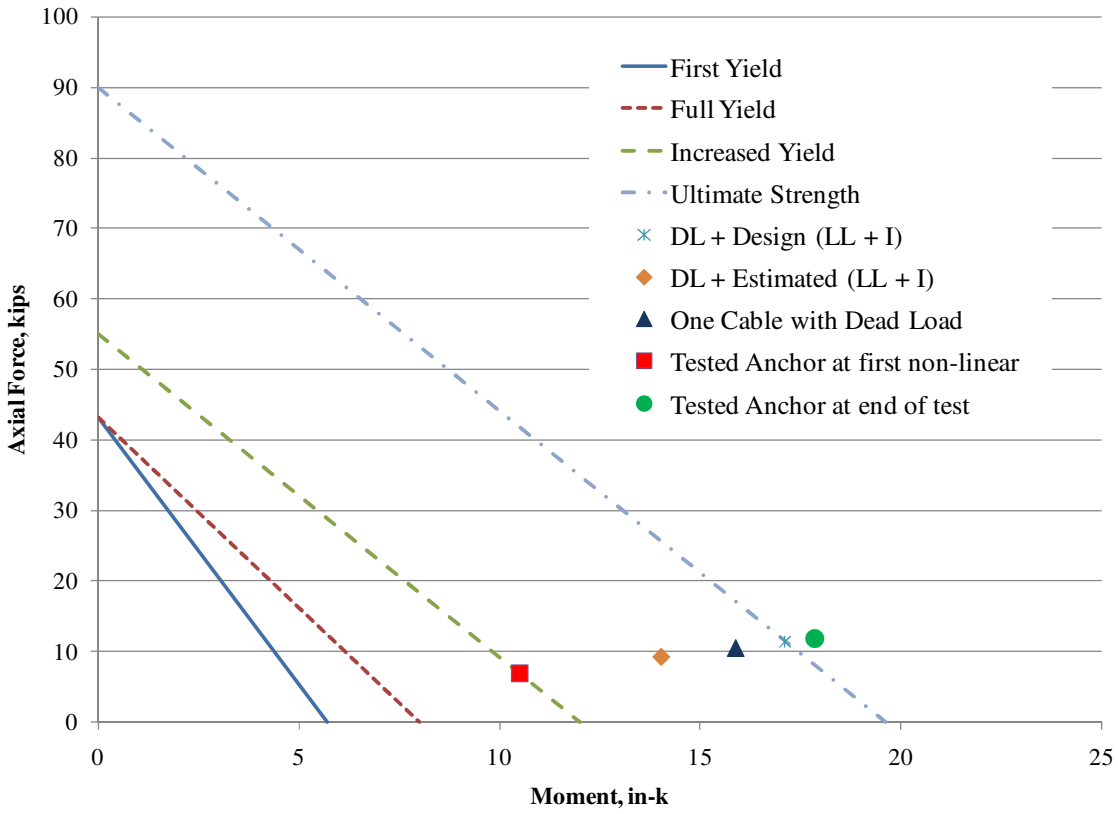

Figure 18. Moment - Axial Force Interaction Diagram

The axial force and moment combination assumed to be on the bridge at the time of collapse falls between the increased yield line and the ultimate strength line. This reinforces Dr. Wright's conclusion that, at the time of failure, the bar had experienced a small amount of ductile yielding, but premature fracture was initiated by the presence of the flaw.

Finally, note that the cable that remains at the bridge site has a calculated axial force and moment, based on 1 ½ in. eccentricity, that falls between the increased yield line and the ultimate strength line. Photographs of the existing anchors (see the 37 degree backstay anchor in Figure 4) indicate that the anchor has opened significantly. The degree of opening of the 37 degree back stay anchor is similar to that seen in the tested anchor in Figure 14(i) at a load of 11.9 kips. This is higher than the calculated load of 10.6 kips (see Table 2), but there may have been a dynamic load effect at the time of collapse. This would have caused the anchor to temporarily see a higher load than 10.6 kips, and exhibit larger deformations, accordingly.

CONCLUSIONS

Based on the analysis and testing performed and described in this report, it can be concluded that the anchor rod would have had more than adequate capacity to carry the loads on the bridge on the day of failure, even considering dynamic load amplification caused by swinging or shaking the bridge, if there had been no eccentricity of load on the hook. With the hook eccentricity, the anchor still was adequate if there had been no flaws in the material. The higher than typical pedestrian load, combined with dynamic amplification, the eccentricity of the load, and the presence of the flaw, all contributed to the failure of the anchor rod and the collapse of the bridge.

RECOMMENDATIONS

Based on the performance the Giles County pedestrian bridge the following recommendations are made to VDOT:

1. *Determine which other suspension bridges in the state use the open hook anchor bolt detail.*

2. D*evelop a method to modify the open hook detail to prevent it from opening under an extreme loading event, should one take place.*

3. *Future construction of pedestrian bridges of similar design should not use the open hook detail.*

4. *Post a maximum number of people allowed on a bridge at one time.*

ACKNOWLEDGMENTS

The authors would like to acknowledge and thank the Salem District crews for their assistance in making measurements of the bridge and retrieving the specimens for testing.

The methods, findings, and data presented in this publication are those of the authors and investigators and not necessarily those of the State of Virginia Department of Transportation.

REFERENCES

Hibbeler, R. C. (2004). Structural analysis. Upper Saddler River, N.J. :, Prentice Hall.

Virginia Department of Transportation Structure and Safety Inspection Report **0359000-**000000000008509 (May 23, 2007). Structure and Bridge Division, Central Office, Richmond, VA.

APPENDIX A

Giles County, VA
Pedestrian Bridge Collapse

ANCHOR ROD FAILURE ANALYSIS

November 24, 2008

William Wright Ph.D., P.E.

Turner-Fairbank Highway Research Center
McLean, VA

TABLE OF CONTENTS

INTRODUCTION

This report presents results of failure analysis testing that was performed on a failed anchor rod from a pedestrian bridge in Giles County, Virginia. Figure 1 shows the failed anchor rod before it was removed and sent to the Turner-Fairbank Highway Research Center (TFHRC). The hook portion of the anchor rod was not recovered and could not be examined.

The fracture surface of the rod was examined using both optical and scanning electron microscopes to provide insight into the cause of failure. The anchor rod was also subjected to a series of destructive tests to determine the strength, toughness, and chemical composition. Finally, a fracture mechanics analysis was performed based on several assumptions concerning cable force at the time of fracture.

Figure 1 Failed anchor rod in-situ prior to removal for laboratory examination and testing.

Figure 2 shows the failed anchor rod section that was delivered to TFHRC. After a preliminary visual examination, the rod was sectioned into five pieces for further testing as shown in figures 2 and 3.

Figure 2 Section of failed anchor rod for failure analysis.

The following tests were performed on the various pieces:

A) Fractographic examination of the fracture surface.
B) Macro-etch section examination of grain structure and micro-hardness testing
C) Sample for chemical analysis
D) Two standard Charpy Vee-Notch test specimens.
E) Tension test

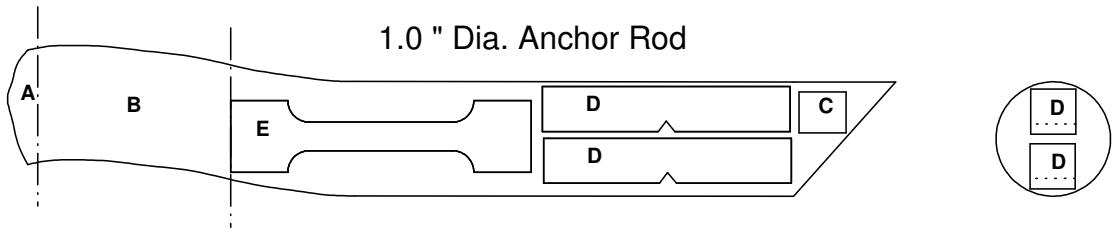

Figure 3 Cut plan for test coupons sectioned from the anchor rod.

MATERIAL PROPERTIES

Chemical Composition

A small sample of material was cut from the interior of the anchor rod at location C. Care was taken to avoid contamination of the sample from the zinc coating on the hook. The sample was sent to Luvak, Inc. for analysis of chemical composition.

It is not known what specification, if any, governed manufacture of the hooked anchor rod. Lacking better information, it is reasonable to assume that the ASTM F 1554 Standard Specification for Anchor Bolts, Steel, 36, 55, and 105 ksi Yield Strength provides a reasonable basis to assess the quality of the anchor rod. Table 1 shows the elemental analysis of the anchor rod compared to two grades from the F 1554 specification.

Table 1 Chemical analysis of the hook rod steel compared to the F 1554 specification.

Element	Anchor Rod Sample "C" (%)	ASTM F 1554 Grade 36 (%)	ASTM F 1554 Grade 55 (%)
Carbon	0.268	0.30 max	...
Manganese	0.69	0.54 min - 0.98 max	...
Sulfur	0.026	0.06 max	0.058 max
Phosphorous	0.033	0.05 max	0.048 max
Silicon	0.18	...	...
Copper	0.35	0.18 min	0.18 min
Nickel	0.12	...	...
Lead	0.003	No intentional addition permitted	No intentional addition permitted
Molybdenum	0.025	...	...
Vanadium	0.003	...	...

In general, the anchor rod conforms to all chemistry requirements specified in ASTM for anchor bolts. Sulfur and Phosphorous are below the specified maximum levels. Carbon and Manganese are within the limits set for F 1554 grade 36. It can also be seen the anchor rod contains significant amounts of Copper and Nickel, presumably to enhance corrosion resistance. It can be concluded that there is nothing abnormal in the chemical composition of the anchor rod that would impair its fitness for purpose as a galvanized anchor bolt.

Strength

One sub-size tension test coupon was machined from the anchor rod with the dimensions shown in figure 4. The specimen was machined to test the material at the center of the anchor rod where any effect of bending will be negligible.. The coupon was tested at a slow constant stroke rate of 0.004 in/min., resulting in a stress rate of about 17.3 ksi/min. This is slightly above

the lower limit for stress rate specified in ASTM A 370 for determination of yield strength (10 to 100 ksi/min). The rate was held constant throughout the test, resulting in a slower strain rate than specified to obtain the tensile strength. The tests were performed at room temperature (about 74°F)

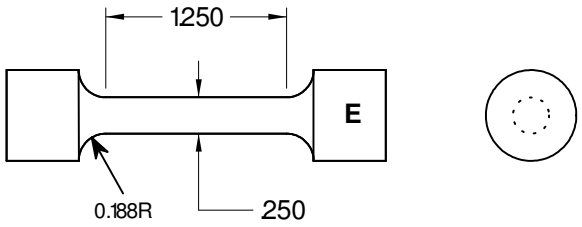

Figure 4 Sub-size tension test coupon providing a gage length four times the diameter.

An extensometer with a one-inch gage length was not available for testing, therefore two strain gages were installed on the specimen to record strain in the early portion of the test. The stroke was measured during the entire test, but this cannot be directly converted to strain since it includes elongation of the specimen and load fixtures outside the gage length. The engineering stress-strain curve shown in figure 5 was constructed from strain gage data below 15,000 με. The portion of the curve exceeding 15,000 με was constructed from the stroke data scaled to match the measured elongation at the end of the test. The exact shape of the curve in the strain hardening portion of the test may contain some small errors relative to the strain axis, but is accurate in terms of stress magnitude.

Figure 6 shows a zoomed-in view of the stress-strain curve showing the calculation of the 0.2% offset yield strength. The test exhibited a pronounced upper yield strength that dropped off suddenly when yielding began. The yield plateau steadily decreased until the point where strain hardening initiates. This behavior is somewhat different compared to grade 50 structural steel tested at similar slow loading rates. Grade 50 structural steels typically have a less pronounced upper yield point and a relatively level yield plateau that favors stable plastic deformation of the material at yield. The sudden drop off in strength at first yield in the anchor rod material will tend to favor unstable plastic collapse and fracture rather than stable elastic-plastic behavior.

Table 2 shows the tension test results compared to the specified strength in the F 1554 specification. It appears that the anchor rod meets the strength requirements of F 1554 grade 55. The 0.2% offset yield strength would probably have exceeded 55 ksi if the test rate was increased to the upper bound allowed by ASTM.

Table 2 Tension Test Properties.

	UYS Upper Yield Point (ksi)	LYS Lower Yield Point (ksi)	σ_{YS} Yield Strength (0.2% Offset) (ksi)	σ_{TS} Tensile Strength (ksi)	Percent Elongation (1 in Gage)[a] (%)
Anchor Rod	**59.03**	**54.84**	**54.20**	**87.78**	**23.9**
F 1554 Grade 55	**...**	**...**	**55.0**	**75 to 95**	**21[b]**
F 1554 Grade 36	**...**	**...**	**36.0**	**58 to 80**	**23[b]**

a) Estimated from final measurements of the total reduced area section of the specimen. Was not directly measured over a 1.0 in gage length.
b) Specified for a 2 in. gage length.

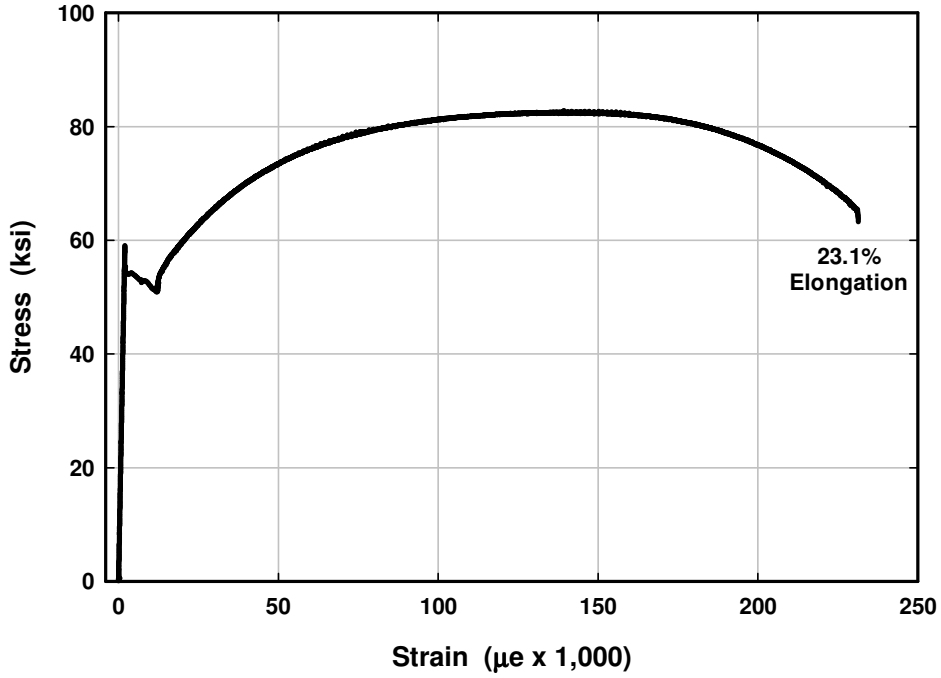

Figure 5 Stress-strain curve constructed from the strain gage and stroke data recorded during testing.

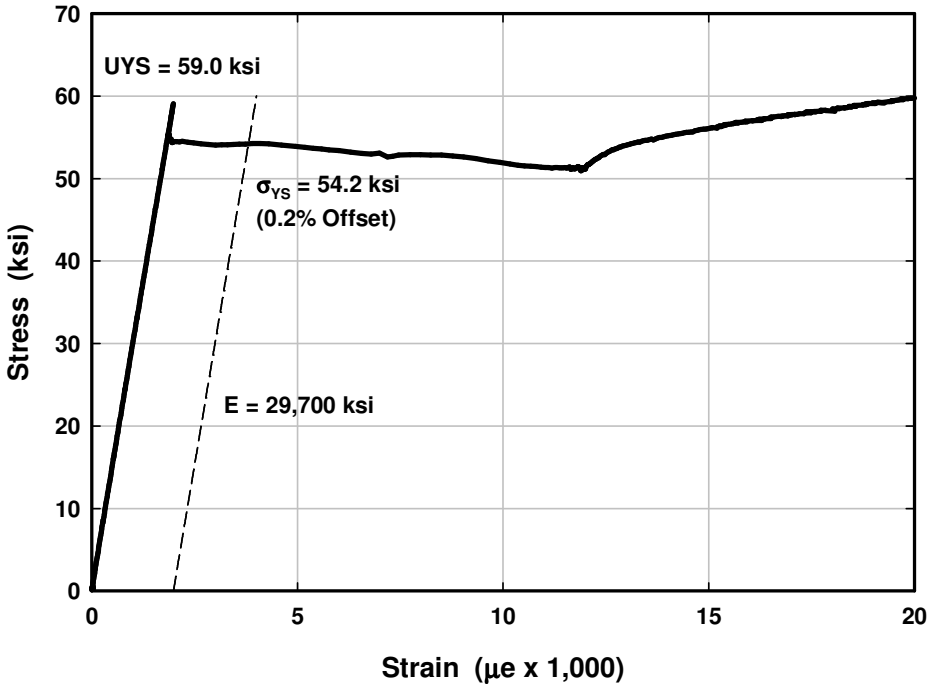

Figure 6 Zoom view of stress-strain curve showing calculation of the 0.2% offset yield strength.

Fracture Resistance Based on Charpy Vee-Notch Data

Two CVN tests were performed in the longitudinal direction (LT) to measure fracture toughness. As shown in figure 3, the test specimens were cut from a straight section of the anchor rod and should be unaffected by bending during fabrication of the hook. The two replicate tests showed similar results as shown in table 2.

Table 2 Estimated fracture resistance from CVN data.

Orientation	CVN Energy (ft-lb)	Test Temperature (°F)	Lateral Expansion (in)	Percent Shear (%)
TL	14.6	40	0.061	29
TL	15.2	40	0.062	31
Averages				
TL	14.9	40	0.0615	30

For reference, the A 1554 Specification S4 supplemental toughness requirement is 15 ft-lb @ +40°F for the average of three replicate specimens. Although two replicate specimens do

not constitute a valid test according to the specification, it appears that the anchor rod essentially meets the S4 toughness requirement.

The dynamic fracture resistance of the plates can be estimated from the CVN results based on the following correlation reported by Barsom & Rolfe (1987):

$$K_{Id} = \sqrt{5(CVN)E} \quad \textbf{(1)}$$

A temperature shift must be applied to obtain the static plane strain fracture initiation resistance K_{Ic}:

$$T_{shift} = 215 - 1.5\, s_{YS} \quad \textbf{(2)}$$

Applying equations 1 and 2, the static fracture initiation resistance of the anchor rod can be estimated as K_{Ic} = 47.0 ksi-in$^{1/2}$ @ -94°F. Toughness will be expected to increase as a function of temperature, but the shape of the toughness transition curve is not known for this steel. Therefore, it can be concluded that the static fracture resistance of the anchor rod at failure exceeded 47 ksi-in$^{1/2}$, but the actual fracture resistance is not known. This result only applies to areas where the anchor rod material is not altered by cold bending or local embrittlement.

Hardness of Hook Bend

"Piece B" shown in figure 3 was sectioned longitudinally and polished to create a macro-etch specimen through the mid-plane of the anchor rod in the bending plane of the hook. The surface was polished and etched with Nital to reveal the grain structure. Micro hardness profiles were measured from the top to bottom of the rod at two locations: 1) toward the left end of the rod close to the fracture location where bending is near it's maximum from the hook radius; and 2) toward the right end where the rod where bending is minimal near an inflection point with minimal curvature.

Figure 7 shows the variation in Vickers hardness across the rod at two cross-sections. Some replicate tests were performed at the curved cross section near the inside edge to verify the peak hardness readings. Tests were performed at 1 mm intervals across the surface, starting 1 mm away from the interface between steel and the galvanized layer. For comparison, the dashed line shows the hardness that would be expected for a steel with 88 ksi tensile strength according to the ASTM A 370 specification. The hardness measurements near the center correlate well with the tension test results. There is a definite increase in hardness toward both surfaces of the rod. The highest hardness is observed close to the inside edge (inner radius) at the cross section with maximum curvature near the fracture location. The Vickers hardness of 279 approximately correlates to a tensile strength of 128 ksi, a 45 % increase relative to the center of the anchor rod.

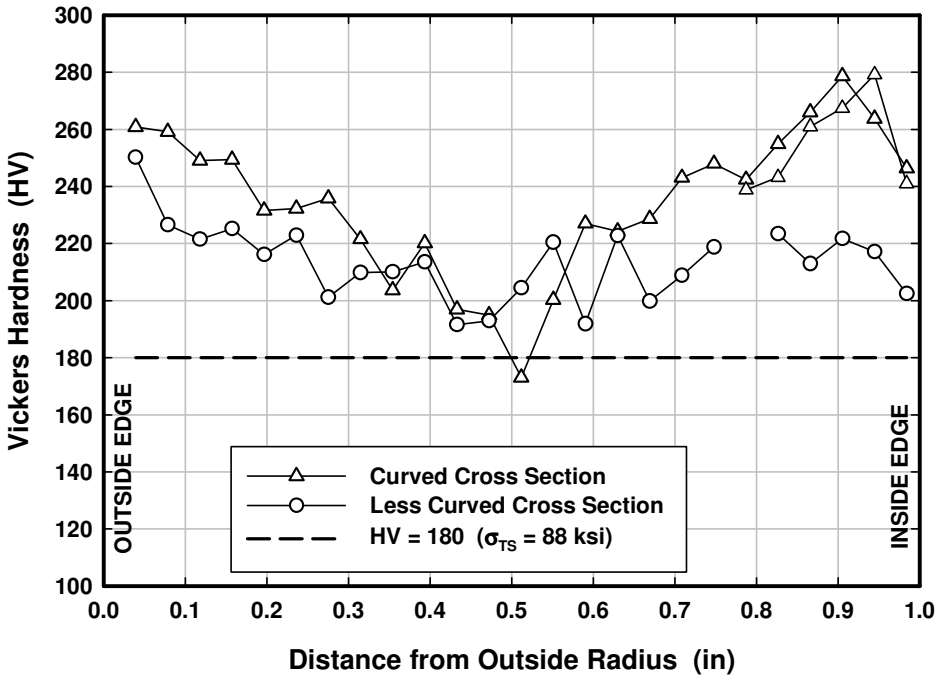

Figure 7 Hardness profile through the center of the rod in the bending plane of the hook.

While the reason for the increased hardness is not precisely known, the pattern suggests strain aging as a possible cause. The curved cross section shows higher surface hardness compared to the less curved section. It also shows more hardening occurs on the inside of the bending radius where the highest strain occurs in bending of curved beams. Strain aging typically increases both the yield and tensile strength by similar amounts. Therefore, it is reasonable to assume a 45% increase in yield strength at the surface, increasing the surface yield stress to 54.2 x 1.45 = 78.6 ksi.

FRACTOGRAPHY

A cylindrical slice of the anchor rod (piece "A") was examined to determine the nature of the fracture. Prior to examination the piece was cleaned in an ultrasonic bath of methyl-ethyl ketone (MEK) to remove the clear coating applied at the bridge site to protect the fracture surface.

Optical Examination

Initial examination revealed a small semi-circular defect originating at the surface of the anchor rod along the inside of the bend radius. Figure 8 shows the presence of chevron lines on the fracture surface radiating away from the defect. This is typical in brittle fracture and the chevron lines point to the defect as the fracture initiation site.

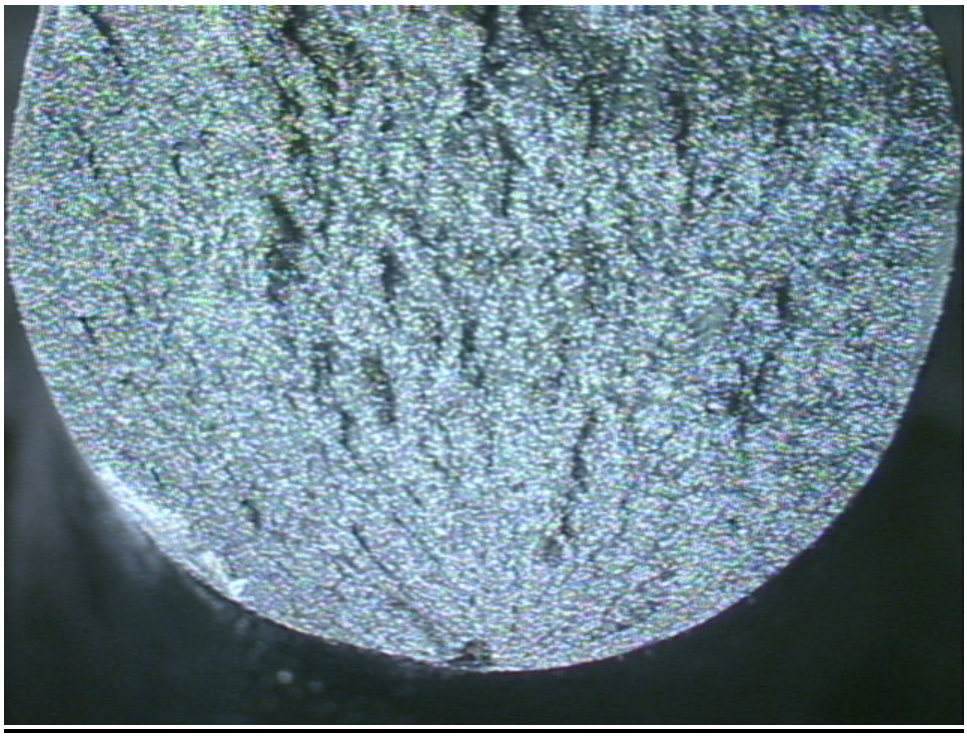

Figure 8 Fracture surface showing chevron lines radiating from a small flaw at the bottom of the photo.

Figure 9 shows a close-up view of the defect looking at the fracture surface. A 15 mil deep corrosion pit is present on the surface of the rod that appears to have developed underneath the galvanized coating. There are two darker semi-circular crack-like defects that appear to have initiated from the corrosion pit. The darker color indicates light surface discoloration compared to the brighter overall fracture surface. This indicates the crack-like defects existed prior to fracture of the rod. The larger semi-circular defect on the right of figure 9 (Crack "A") measures about 29 mil deep from the rod surface. The smaller defect on the left (Crack "B"), extends

about 14 mils deep. It was unclear from optical examination if the defects are separate or coalesced together. Note that the optical digital microscope used to take the images in figures 8 through 11 inverts the image compared to the SEM images in the following section.

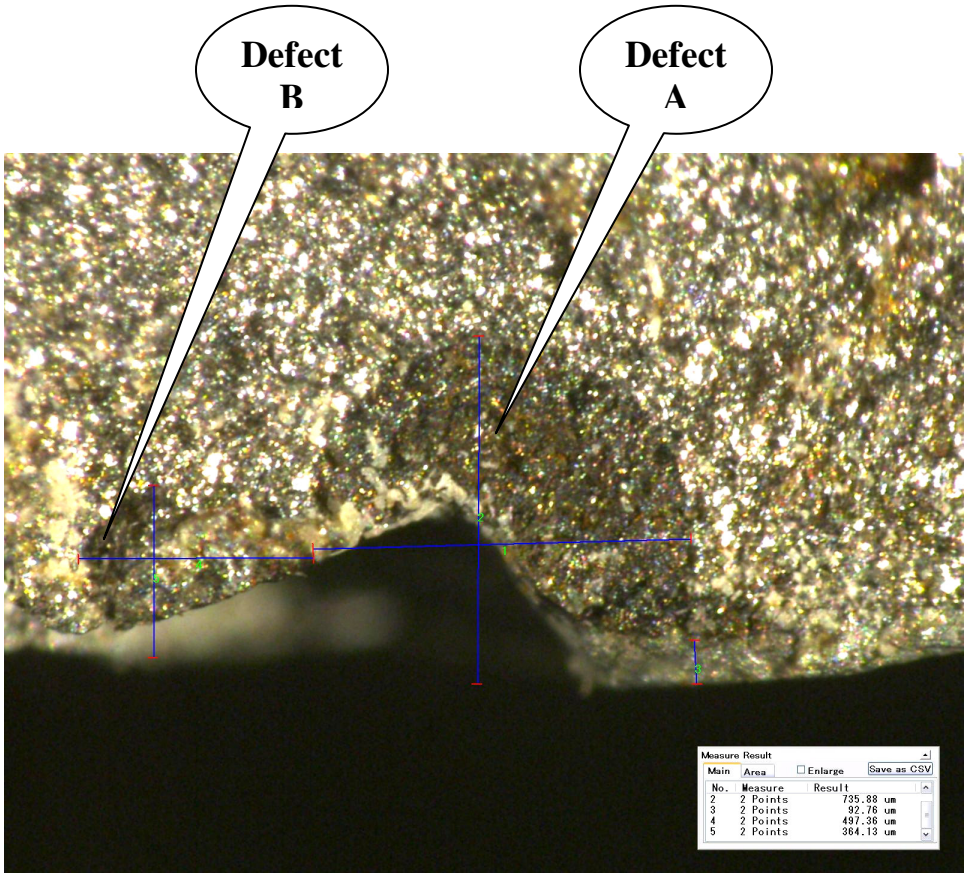

Figure 9 Close-up view of the crack-like defect originating from the corrosion pit. (150X)

Figure 10 shows the galvanized surface of the anchor rod at the edge of the fracture. A corrosion pit measuring about 0.037 in. is apparent on the surface of the rod. The dark center region is a deep brown color indicating corrosion on the steel surface. The lighter ring around the center is a conical break through the thickness of the galvanized coating. The conical surface area is much brighter than the galvanized surface of the rod, indicating that this surface is newer and has been exposed to less weathering. It is likely that a corrosion cell developed under the surface of the galvanized coating and eventually created pressure that caused a conical break through the surface. It cannot be determined if this surface break existed prior to the fracture of the rod or occurred during the fracture.

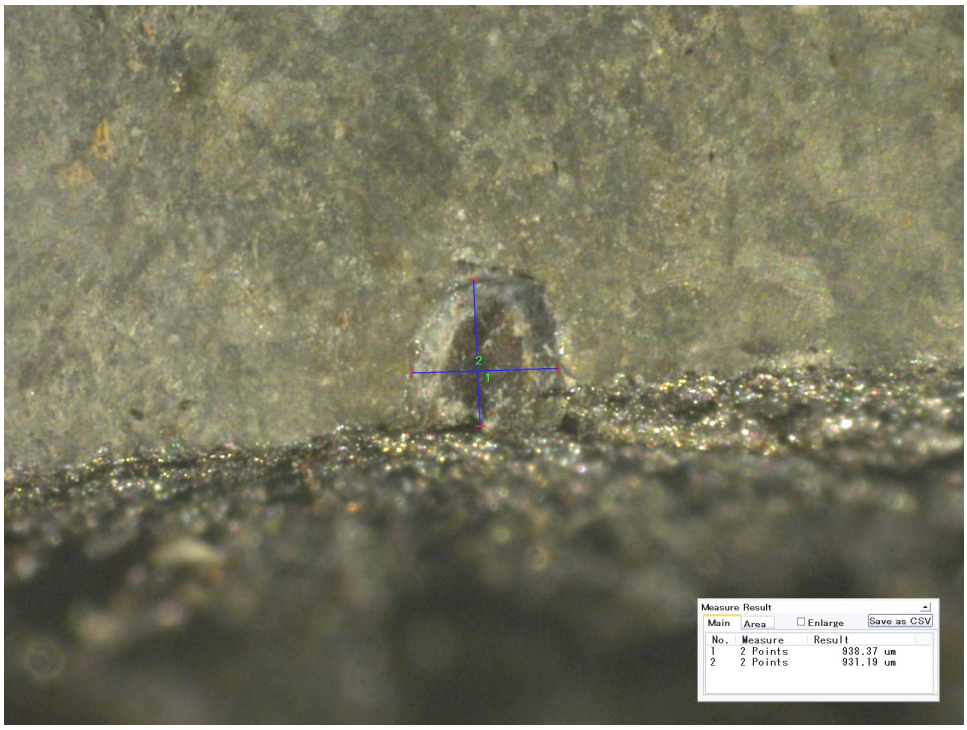

Figure 10 Surface of the hook rod showing a corrosion pit with diameter about 0.037 in. (50X)

Figure 11 shows a view of the fracture surface adjacent to the defect showing the galvanized coating. There is some local variability in thickness, but on average the galvanized coating is about 3.5 mils thick. Figure 12 shows the surface of the anchor rod along the inside of the bend radius. The fracture surface is to the left of the figure. A series of short transverse cracks appear to be present on the galvanized surface. There is some minor evidence of rust bleeding around some of the surface cracks, indicating the possible presence of sub-surface corrosion. These cracks were only apparent on the inside bend radius. There was no evidence of cracking along the outside bend radius or along the sides of the anchor rod.

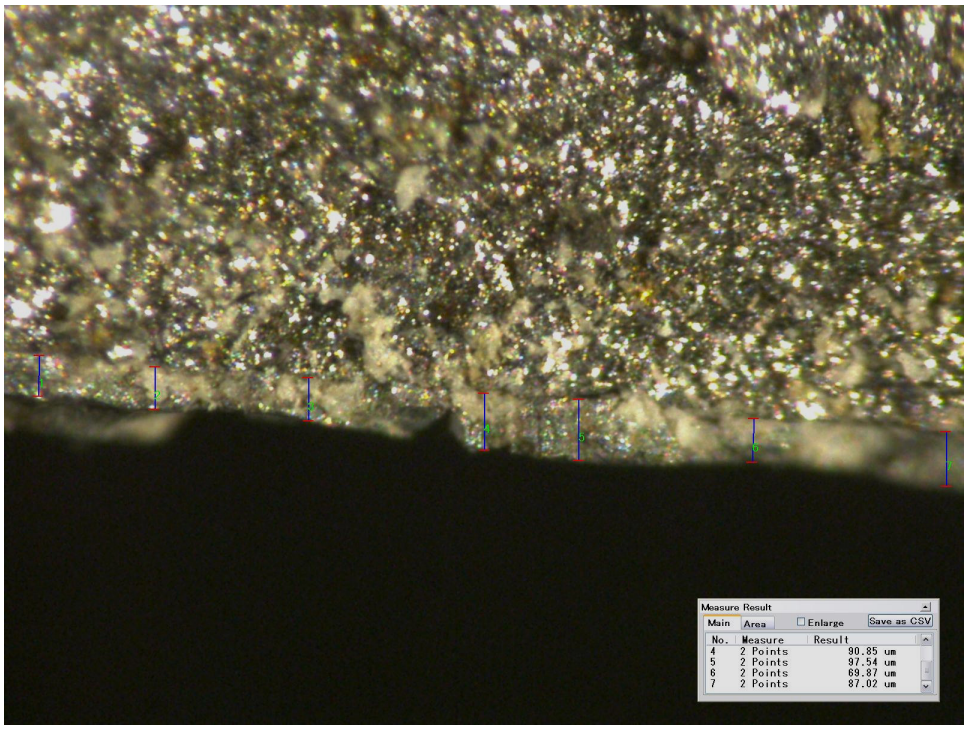

Figure 11 Measurements of the galvanized coating thickness adjacent to the crack-like defect indicating about a 3.4 mil average thickness. (150X)

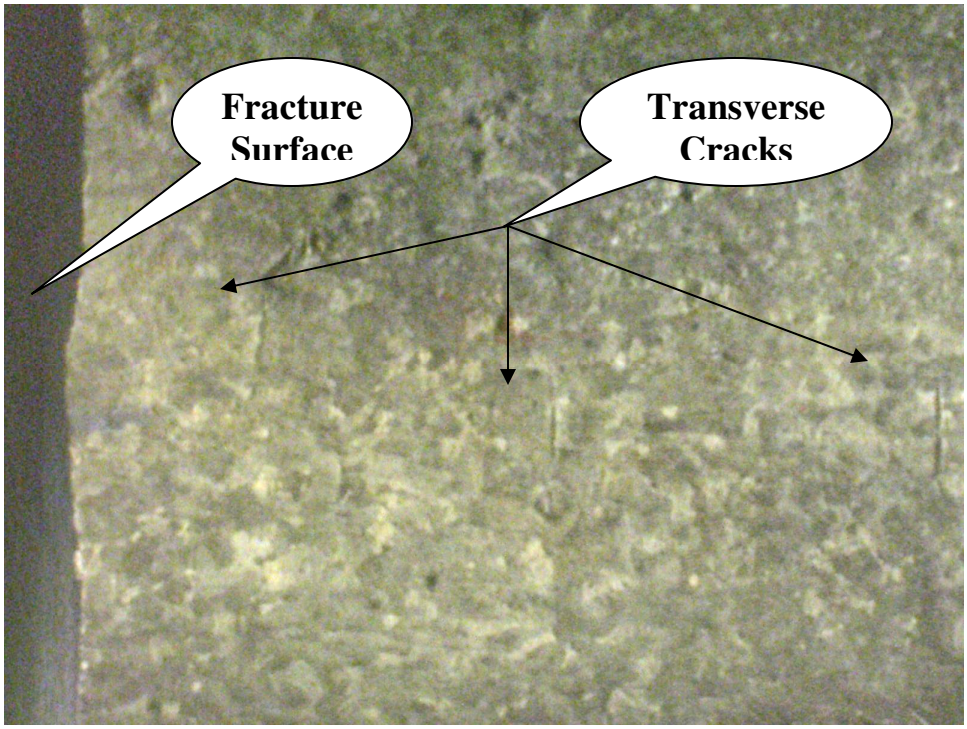

Figure 12 Surface of the anchor rod along the inside of the bend radius showing a number of small transverse cracks on the galvanized surface. (20X)

Scanning Electron Microscopy (SEM)

A ½" square piece of the fracture surface containing the initial defect was mounted and examined under a scanning electron microscope (SEM). Figure 13 shows a low power view of the crack-like defect that was determined to be the fracture initiation site. The locations for the following close-up images are shown in the figure. Virtually the entire surface of the crack-like defects was examined during the scanning procedure. The following close-up images can be considered typical.

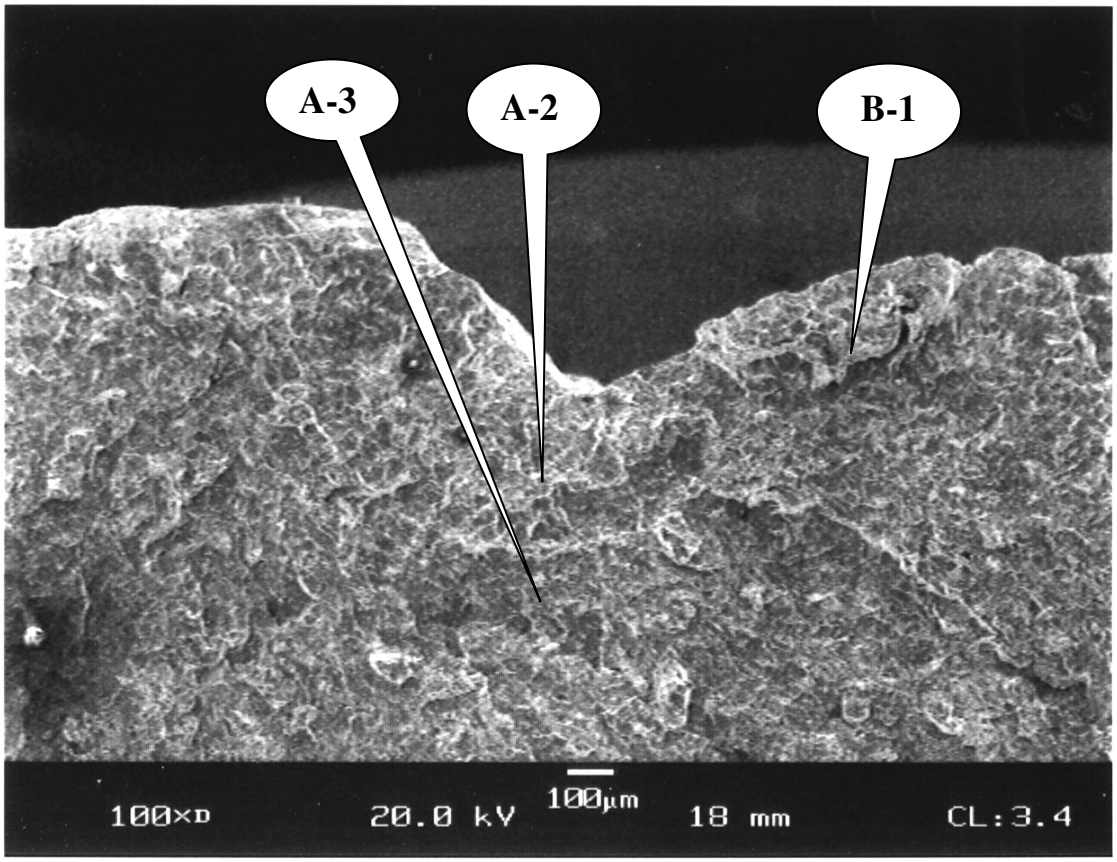

Figure 13 Location of close-up locations for SEM figures.

Figures 14 and 15 show the fracture surface at location A-2 in the middle portion of defect A. The surface appears to have a combination of inter-granular and trans-granular cleavage cracking. In some locations, there is evidence of inter-granular cracks extending into the material from the crack surface. There is also evidence of corrosion on the crack surface at random locations. No evidence of fatigue striations could be found on the surface. Cyclic loading could have contributed to the gradual propagation of inter-granular cracking (corrosion fatigue) but fatigue does not appear to be the primary cause of cracking.

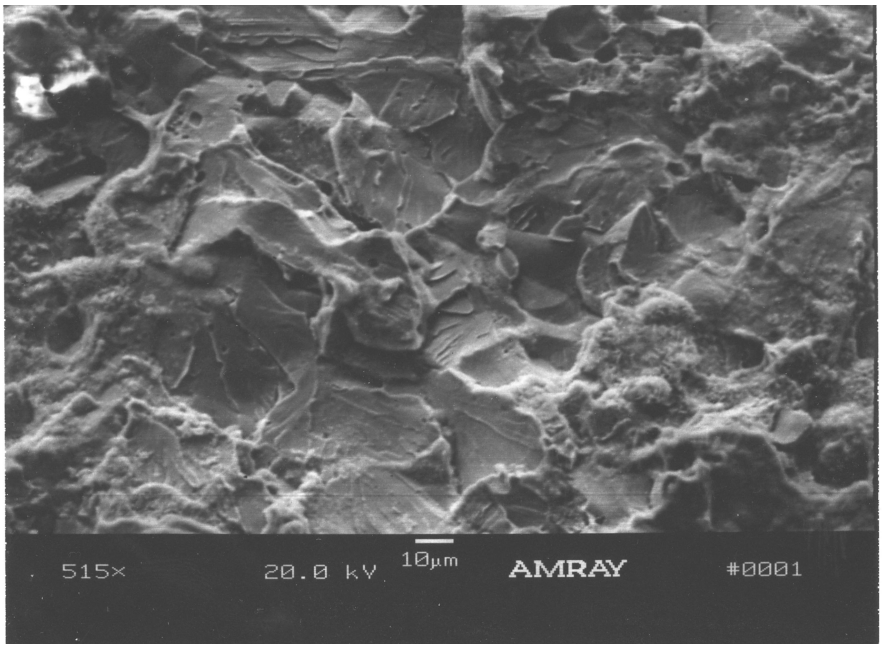

Figure 14 Location A-2 showing a combination of inter-granular fracture and trans-granular cleavage.

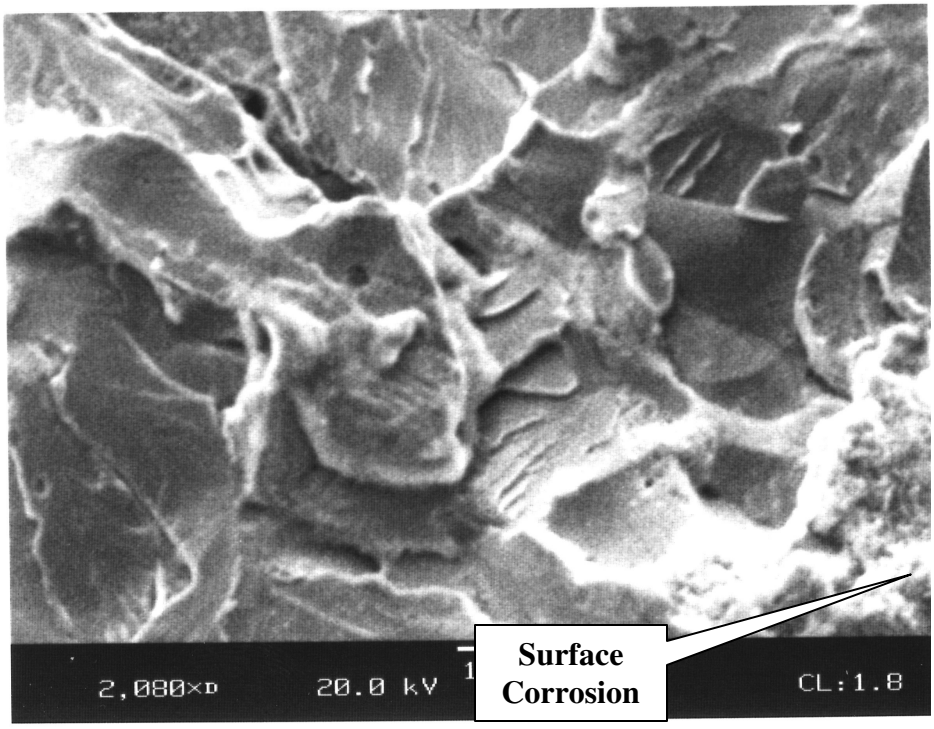

Figure 15 Location A-2 showing area of surface corrosion.

Figure 16 shows the semi-circular boundary of the crack-like defect at location A-3. A distinct area of ductile fracture is evident around the circular boundary of the defect. The conical dimples are typical for material that fails by micro-void coalescence with significant plastic deformation prior to fracture. The area below the circular boundary is brittle trans-granular cleavage fracture. This is typical for the entire fracture surface outside of the circular boundary. There is no corrosion evident on the fracture surface outside of defect A indicating it was not exposed for long to the environment.

Except near the surface of the anchor rod there was no evidence of elemental zinc on the fracture surface. The presence of zinc on the crack face near the surface is questionable since the EDAX scan may have been picking up zinc from the galvanized coating.

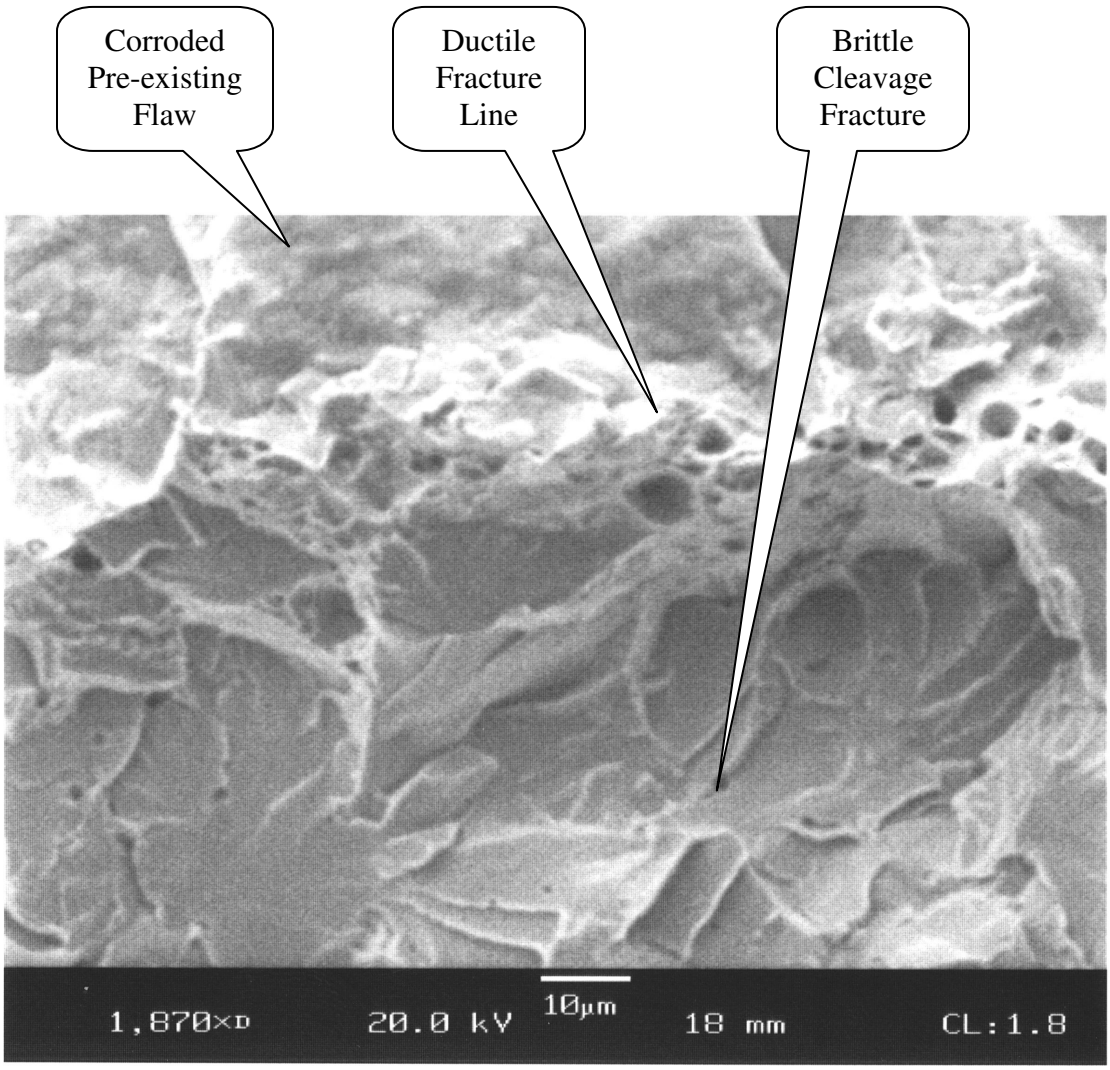

Figure 16 Location A-3 showing ductile fracture at the transition between the preexisting defect and the brittle fracture surface.

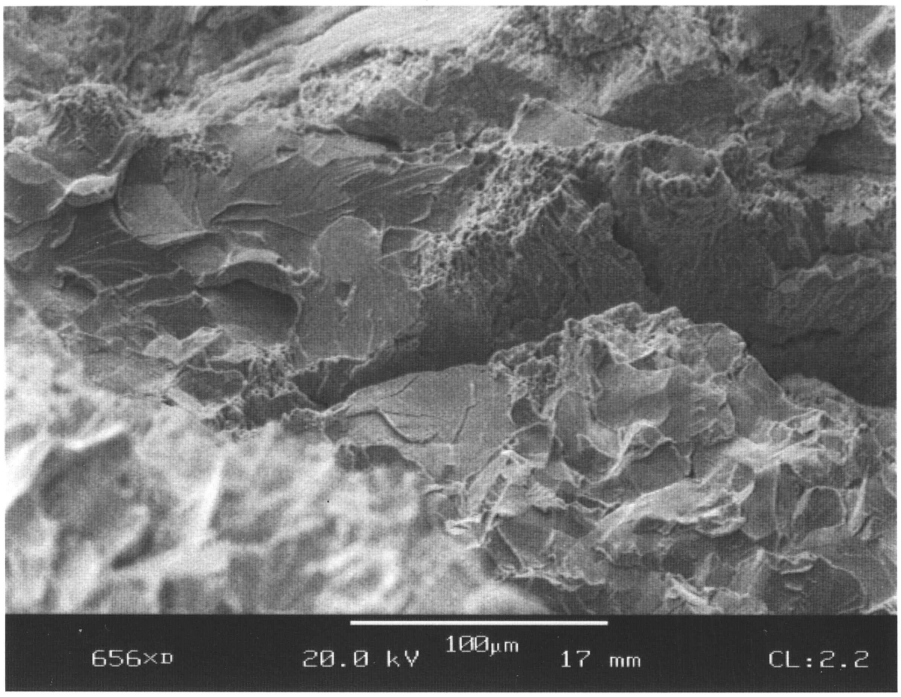

Figure 17 Inter-granular cracking at location B1

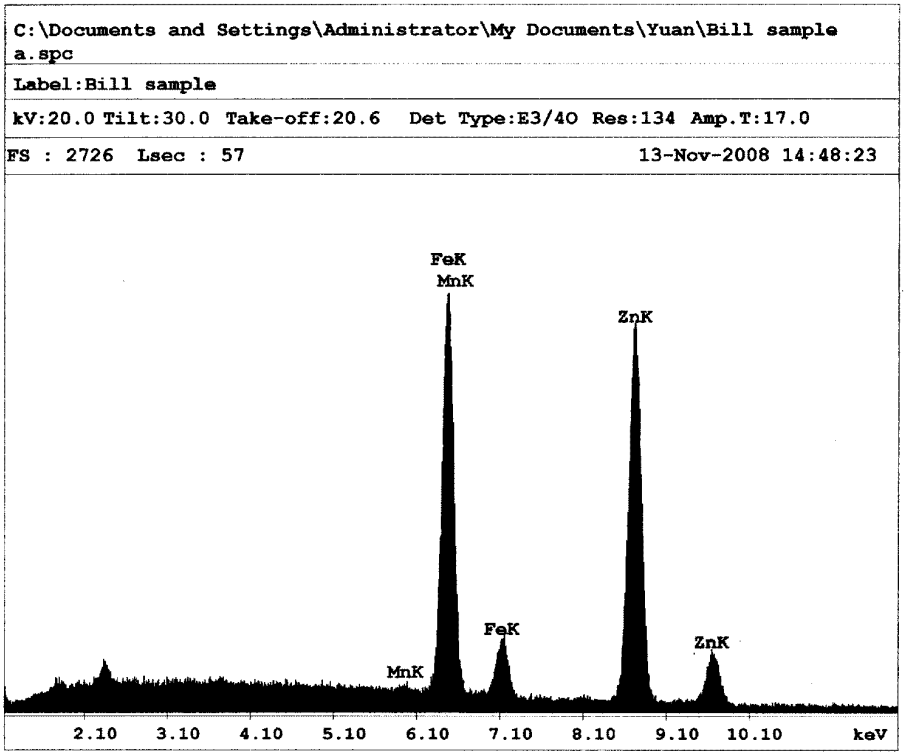

Figure 18 EDAX elemental analysis of surface of the inter-granular crack shown in figure 17.

Figure 17 shows an area close to the surface of the anchor rod in defect B. In general, defect B seemed to have more pronounced inter-granular cracking and the areas of corrosion seemed to concentrate around the inter-granular cracks. This suggests that random inter-granular cracking preceded formation of the semi-circular crack-like defect.

Figure 18 shows results from an X-ray diffraction (EDAX) elemental analysis of the surface inside the inter-granular crack. As expected, the results indicate the presence of iron and manganese. However, there is also a significant presence of zinc suggesting that the trans-granular crack existed prior to galvanizing. This was observed in multiple locations in defect B.

Interpretation of Fractography

The two crack-like defects appear to have existed prior to the main fracture of the anchor rod. The nature of the defects cannot be positively determined but there is no evidence of fatigue. There is evidence of inter-granular cracking which is consistent with local embrittlement of the metal. There is also evidence that some inter-granular cracking existed prior to galvanizing of the anchor rod. The most likely scenario is that the crack-like defects developed as pop-in type fractures from areas of embrittlement around the inter-granular cracks. The pop-in fractures likely arrested at the semi-circular perimeter of the crack-like defect. The

defect then appears to have existed for some time in the anchor rod prior to the main fracture event.

The presence of significant crack blunting (ductile yielding) can be clearly observed around the circular perimeter of the crack-like defects. This indicates an elastic-plastic condition existed at the crack tip prior to fracture. One possibility is that the plastic deformation occurred due to crack arrest. This is doubtful given that the semi-circular defect is constrained by the surrounding un-cracked material which would have to undergo significant yielding to maintain deflection compatibility with the crack tip deformation. The more likely cause is that the anchor rod with the crack-like defect was subjected to a high stress level, resulting in large elastic deformation and yielding of the material along the inside radius of the anchor rod. The blunting at the crack tip had to occur in compatible deformation with the surrounding material.

The main fracture surface is entirely trans-granular cleavage indicating a brittle instability failure. Even though the local conditions at the crack tip were ductile, the main fracture was brittle. The material clearly did not have sufficient toughness to support stable ductile crack extension. As shown in figure 5, the shape of the stress-strain curve indicates a sudden drop in yield strength after the upper yield strength is reached. Since the applied load is constant, the drop in yield strength will tend to drive the fracture toward instability.

FRACTURE ANALYSIS

A fracture mechanics analysis of the anchor rod was performed using MathCAD as shown in Appendix A. This was intentionally performed with no knowledge of the actual loading present in the structure. The dimensions of the anchor rod were estimated by measuring a photograph of one of the anchor hooks that did not fail. There appears to be about a nine degree difference between the line of action of the cable and the base of the anchor hook. Since the hook is not closed, bending stress dominates the section where fracture occurred. The calculations in Appendix A show a sketch of the estimated hook dimensions and the non-linear stress distribution inherent in bending of curved beams.

The force in the suspension cable is not exactly known at the time of failure, but the calculations show that a force of 2,551 lbs will cause a surface tensile stress on the inside radius of the hook equal to the yield strength of the base material. The defect shown in the previous section is located on the inside radius at the location of maximum tensile stress.

Several assumptions were made to determine the stress intensity factor K_I at the defect under the 2,551 lb cable load. Defects A and B were assumed to be a single larger defect that can be modeled as a single semi-elliptical surface flaw with depth $a = 0.029$ in. and width $2c = 0.048$ in. The stress intensity factor solution for a semi-elliptical surface flaw in a plate with rectangular cross section was employed to model the crack (Newman & Raju, 1981). Since the defect is small relative to the diameter of the anchor rod, any difference between the circular and rectangular cross sections will be minimal.

Results show that the stress intensity factor at the defect is only $K_I = 12$ ksi-in$^{1/2}$ when the surface stress in at yield in the anchor hook. Since the fracture resistance of the base material $K_{Ic} > 47$ ksi-in$^{1/2}$ at the service temperature at the time of failure, fracture initiation would not be expected from the defect under either static or pseudo-dynamic load rates.

The hardness readings indicate higher strength material at both the inside and outside radii of the hook bend. Assuming the yield strength increases proportionally with the tensile strength, the yield stress of the material around the defect could have been as high as 79 ksi. Repeating the calculations in Appendix A would indicate it would take a cable force of 3,750 lbs. to reach this stress level. The stress intensity factor at the defect would increase to about $K_I = 17.3$ ksi-in$^{1/2}$. This is still well below the fracture resistance of the material and is well below the level that would cause crack tip blunting.

In summary, small size of the defect would not be expected to initiate brittle fracture even with stress levels approaching the yield strength of the material. The presence of significant crack-tip plasticity can only be explained if the material surrounding the defect was yielding prior to the fracture.

CONCLUSIONS

- The anchor rod material, strength, and toughness appear to be consistent with F1554 grade 55 material with added copper and S4 supplemental CVN toughness. This material appears suitable for service as a galvanized anchor bolt.

- The hardness profile across a section of the anchor rod indicates increased strength at the inned and outer bend radii of the rod. This could be caused by strain aging following formation of the rod. It coulds also be caused by strain hardening due to plastic deformation of the rod under load.

- Two small crack-like defects were present on the inside radius of the anchor hook and served as the initiation site for brittle fracture. Two small semi-circular crack-like flaws appear to have initiated from a corrosion pit on the surface of the anchor hook.

- There is some evidence that local embrittlement of the anchor hook was present at the surface around the corrosion pit. Several inter-granular cracks were observed near the surface that have a significant amount of zinc on the crack surface. This indicates that shallow surface cracking may have been present at the time the anchor hook was galvanized.

- The crack-like defects were likely formed by pop-in type fracture from areas of local embrittlement. The perimeter of the defect appears to be defined by arrest of the pop-in fracture in tougher material.

- Fracture mechanics indicates that the initial crack-like defect is too small to trigger brittle fracture with applied stress levels up to the yield strength of the material.

- Fracture appears to have been preceded by yielding and inelastic deformation of the anchor rod material at the inside of the hook radius. This caused significant crack tip yielding that eventually triggered fracture instability.

- The failure appears to have been initiated by an overload that exceeded the yield strength of the anchor rod. The presence of the initial crack-like defect caused the failure mode to transition to brittle fracture after yielding began.

REFERENCES

1) Barsom, J.M., and Rolfe, S.T. (1987) *Fracture and Fatigue Control in Structures*, 2nd. ed., Prentice Hall.

2) Newman, J. C. and Raju, I. S. (1981) *An Empirical Stress-Intensity Factor Equation for the Surface Crack*. Engng. Frac. Mech., Vol. 15, No. 1-2, pp. 185-192.

APPENDIX A - Fracture Calculations

Giles County Anchor Rod Failure
Fracture Analysis of Defect

Curved Beam Solution: Boresi, A.P., and Sidebottom. O.M. (1985) *Advanced Mechanics of Materials*, 4th Ed., J. Wiley & Sons.

$b := \frac{1.0}{2}$

$R := 1.5$

$P := 2551$ lbs

$\phi := 9 \cdot \left(\frac{2 \cdot \pi}{360}\right)$

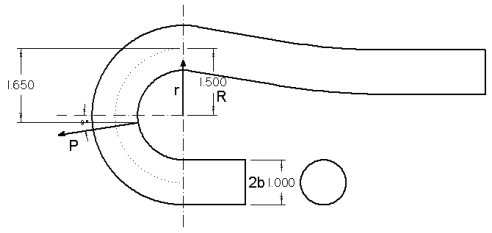

$N := P \cdot \cos(\phi)$ $\quad N = 2.52 \times 10^{3}$ lbs

$M := (1.65 \cdot N) - P \cdot \sin(\phi)$ $\quad M = 3.758 \times 10^{3}$ in – lbs

$A := \pi \cdot b^{2}$

$A_m := 2 \cdot \pi \cdot \left(R - \sqrt{R^{2} - b^{2}}\right)$

$\sigma_{\theta\theta}(r) := \frac{N}{A} + \frac{M \cdot (A - r \cdot A_m)}{A \cdot r \cdot (R \cdot A_m - A)}$ $\quad r := 1, 1.01 .. 2$

$\sigma_{\theta\theta}(1) = 5.42 \times 10^{4}$ psi

$\sigma_{\theta\theta}(2) = -2.707 \times 10^{4}$ psi

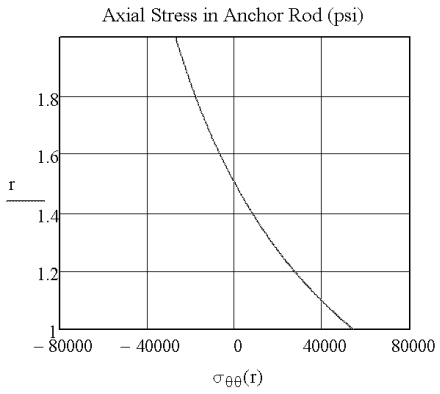

Semi-Elliptical Surface Crack Solution:

Newman, J. C. and Raju, I. S. (1981) *An Empirical Stress-Intensity Factor Equation for the Surface Crack*. Engng. Frac. Mech., Vol. 15, No. 1-2, pp. 185-192.

$\sigma_m := \frac{P}{A}$ $\quad \sigma_m = 3.248 \times 10^3$ psi *Axial Stress*

$\sigma_b := \sigma_{\theta\theta}(1) - \sigma_m$ $\quad \sigma_b = 5.095 \times 10^4$ psi *Bending Stress*

$\phi := \frac{\pi}{2}$ *Maximum SIF is at the deepest part of the crack.*

$a := .029$

$c := \frac{0.048}{2}$

$W := 1$

$t := 1$

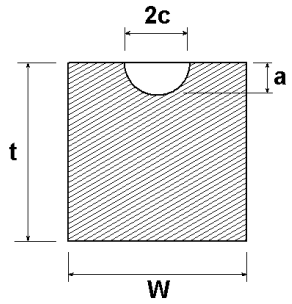

Rectangular Bar Approximation

$M_1 := 1.13 - 0.09 \cdot \left(\frac{a}{c}\right)$ $\quad M_2 := -0.54 + \frac{0.89}{0.2 + \frac{a}{c}}$ $\quad M_3 := 0.5 - \frac{1.0}{0.65 + \frac{a}{c}} + 14 \cdot \left(1.0 - \frac{a}{c}\right)^{24}$

$f_\phi := \left[\left(\frac{a}{c}\right)^2 \cdot \cos(\phi)^2 + \sin(\phi)^2\right]^{\frac{1}{4}}$ $\quad f_\phi = 1$

$f_W := \left(\sec\left(\frac{\pi \cdot c}{2 \cdot W} \cdot \sqrt{\frac{a}{t}}\right)\right)^{\frac{1}{2}}$ $\quad f_W = 1$

$g := 1 + \left[0.1 + 0.35 \cdot \left(\frac{a}{t}\right)^2\right] \cdot (1 - \sin(\phi))^2$ $\quad g = 1$

$F := \left[M_1 + M_2 \cdot \left(\frac{a}{t}\right)^2 + M_3 \cdot \left(\frac{a}{t}\right)^4\right] \cdot f_\phi \cdot f_W \cdot g$ $\quad F = 1.021$

$$Q := 1 + 1.464 \cdot \left(\frac{c}{a}\right)^{1.65} \qquad Q = 2.071$$ *Note: a/c>1*

$$p := 0.2 + \frac{a}{c} + 0.6 \cdot \left(\frac{a}{t}\right)$$

$$H_1 := 1 - 0.34 \cdot \left(\frac{a}{t}\right) - 0.11 \cdot \left(\frac{a}{c}\right) \cdot \left(\frac{a}{t}\right)$$

$$G_1 := 1.22 - 0.12 \cdot \left(\frac{a}{c}\right)$$

$$G_2 := 0.55 - 1.05 \cdot \left(\frac{a}{c}\right)^{0.75} + 0.47 \cdot \left(\frac{a}{c}\right)^{1.5}$$

$$H_2 := 1 + G_1 \cdot \left(\frac{a}{t}\right) + G_2 \cdot \left(\frac{a}{t}\right)^2$$

$$H := H_1 + (H_2 - H_1) \cdot \sin(\phi)^p \qquad H = 1.031$$

Stress Intensity at Bottom of Crack

$$K_I := (\sigma_m + H \cdot \sigma_b) \cdot \sqrt{\frac{\pi \cdot a}{Q}} \cdot F \cdot \left(\frac{1}{1000}\right)$$

$K_I = 11.95$ $\quad ksi \cdot \sqrt{in}$